NOTICE: This is the author's version of a work that was accepted for publication in Computers & Geotechnics. Changes resulting from the publishing process, such as peer review, editing, corrections, structural formatting, and other quality control mechanisms may not be reflected in this document. Changes may have been made to this work since it was submitted for publication. A definitive version was subsequently published in Computers & Geotechnics, 134:104018, 2021. doi.org/10.1016/j.compgeo.2021.104018

Back-analysis of model tests on piles in sand subjected to long-term lateral cyclic loading: impact of the pile installation and application of the HCA model

Patrick Staubach*; Jan Machaček†; Raihan Sharif‡, Torsten Wichtmann§

Abstract: The back-analysis of model tests on piles subjected to high-cyclic lateral loading using the high-cycle accumulation (HCA) model is presented. The installation of the pile prior to the lateral loading is taken into account using a Coupled-Eulerian-Lagrangian method. A comparison between the measured pile rotation and the results of simulations with incorporation of the installation-induced soil changes as well as simulations assuming wished-in-place initial conditions is made. A distinct influence of the installation process on the lateral response of the pile is observed. The installed piles exhibit larger resistance and less accumulation of deformation during the cyclic loading. The simulations taking into account the installation process are in better accordance with the measurements in the model tests compared to the wished-in-place simulations. It is concluded that the consideration of the installation process in a back-analysis of driven piles subjected to monotonic or cyclic loading is of great importance.

Keywords: High cyclic loading, monopile, high-cycle accumulation model, Coupled-Eulerian-Lagrangian, pile installation, large deformation

1 Introduction

Despite being an extensively studied subject in geotechnics, the uncertainty of predicting the pile response to (cyclic) lateral loading remains large. Up to now no state of the art method exists for the estimation of the long-term deformations caused by cyclic lateral loading. A reliable design method is especially important for offshore wind turbines founded on piles as they have only a small tolerance towards tilting and are repeatedly loaded by wind and water waves during their lifetime.

A variety of numerical approaches with varying degrees of complexity have been proposed for the estimation of the pile response to cyclic lateral loading (see e.g. (Achmus et al., 2009; Cuéllar et al., 2014; Kim et al., 2015; Carstensen et al., 2018; Li et al., 2019; Page et al., 2019; Staubach and Wichtmann,

*Chair of Soil Mechanics, Foundation Engineering and Environmental Geotechnics, Ruhr Universität Bochum, Germany/Chair of Geotechnics, Bauhaus Universität Weimar, Germany. Email: patrick.staubach@rub.de, Corresponding author

†Institute of Geotechnics, Technische Universität Darmstadt, Germany/Chair of Soil Mechanics, Foundation Engineering and Environmental Geotechnics, Ruhr-Universität Bochum, Germany

‡Chair of Soil Mechanics and Geotechnical Engineering, Brandenburgische Technische Universität Cottbus-Senftenberg, Germany

§Chair of Soil Mechanics, Foundation Engineering and Environmental Geotechnics, Ruhr-Universität Bochum, Germany

2020; Jostad et al., 2020)). However, the installation process of the pile has not been considered and wished-in-place conditions have been assumed in all cases. As has been shown in (Staubach et al., 2020c; Staubach et al., 2020b), the installation can have a distinct impact on the response of the pile to lateral (cyclic) loading. This is primarily due to a densification and stress increase in the vicinity of the pile tip caused by the installation process (at least for a medium dense initial soil state), leading to a very high base resistance compared to a wished-in-place pile. Depending on the stiffness of the pile itself, the increased soil stiffness at the base caused by the installation increases the overall stiffness of the pile-soil system and lowers the point of rotation of the pile as a higher portion of load is transferred to the stiff soil volume around the tip. Experimental evidence for this phenomenon is also given in (Fan et al., 2019; Fan, 2020), where the response of piles installed in a centrifuge at 1g and 100g, respectively, to subsequent monotonic lateral loading is investigated. As expected, the pile installed at 100g exhibited a higher stiffness when subjected to lateral loading.

In order to investigate the impact of the installation procedure on the numerical back-analysis of small-scale model tests on piles subjected to (high) cyclic lateral loading, the installation and subsequent lateral loading are simulated in the present work. Numerous experimental investigations using small-scale model tests (see e.g. (Leblanc et al., 2010; Yu et al., 2015; Arshad and Kelly, 2017; Rudolph et al., 2014; Richards et al., 2019)) and centrifuge tests (Li et al., 2010; Bayton et al., 2018; Truong et al., 2019) are reported in the literature which are suitable for the present purpose. Being well described and often referred to, the small scale experiments performed by Leblanc et al. (Leblanc et al., 2010) are considered in this work. These tests include monotonic and cyclic lateral loading with up to 20,000 cycles.

To simulate the high-cyclic loading, the high-cycle accumulation (HCA) model (Niemunis et al., 2005) is applied. The HCA model has been validated based on back-analysis of model tests on monopiles and shallow foundations (Solf, 2012; Zachert, 2015) and on a field test on a prototye of a gravity base foundation in 1:1 scale (Zachert et al., 2014; Zachert et al., 2015; Zachert et al., 2020). A back-analysis of centrifuge tests on monopiles reported in (Page et al., 2020) showed a good agreement with the experimental results even if the material parameters of the HCA model were only estimated based on granulometry and simple index quantities. Furthermore, the cumulative deformations measured at a ship lock over two decades were successfully reproduced in simulations with the HCA model (Machaček et al., 2018). The soil improvement by vibro-compaction, which involves several thousands of loading cycles, has also been simulated using the HCA model (Triantafyllidis and Kimmig, 2019; Kimmig et al., 2019).

The HCA model has been used for a parametric study on the long-term deformations of monopile foundations for offshore wind turbines in (Staubach and Wichtmann, 2020). Important aspects such as the influence of the drainage conditions or the ordering of cyclic load bundles with different amplitudes were investigated. The influence of the installation (method) on the long-term behaviour of piles has been investigated using the HCA model in (Staubach et al., 2020c), and in particular for offshore piles in (Staubach et al., 2020b). It was found that the installation-induced changes in the soil state around the pile significantly influence its response to lateral (cyclic) loading. This work aims to validate these findings by the back-analysis of the tests by Leblanc et al. Furthermore, the influence of the installation process on the long-term behaviour of piles is quantified in order to clarify whether it is mandatory to consider the installation-induced changes in the soil state when validating numerical methods using model tests on installed piles.

In order to determine the material constants for yellow Leighton-Buzzard sand, which was used in the model tests of Leblanc et al., an extensive laboratory testing program has been conducted. The calibration procedure is described in detail in this paper. The pile installation is simulated using a Coupled-Eulerian-Lagrangian (CEL) method (upper row in Fig. 1). After the installation, the pile is subjected to a high-cyclic lateral loading, simulated with the HCA model (lower row of Fig. 1). The results

of the simulations taking into account the installation-induced changes in the soil state are compared to results assuming wished-in-place conditions and the measurements in the model tests.

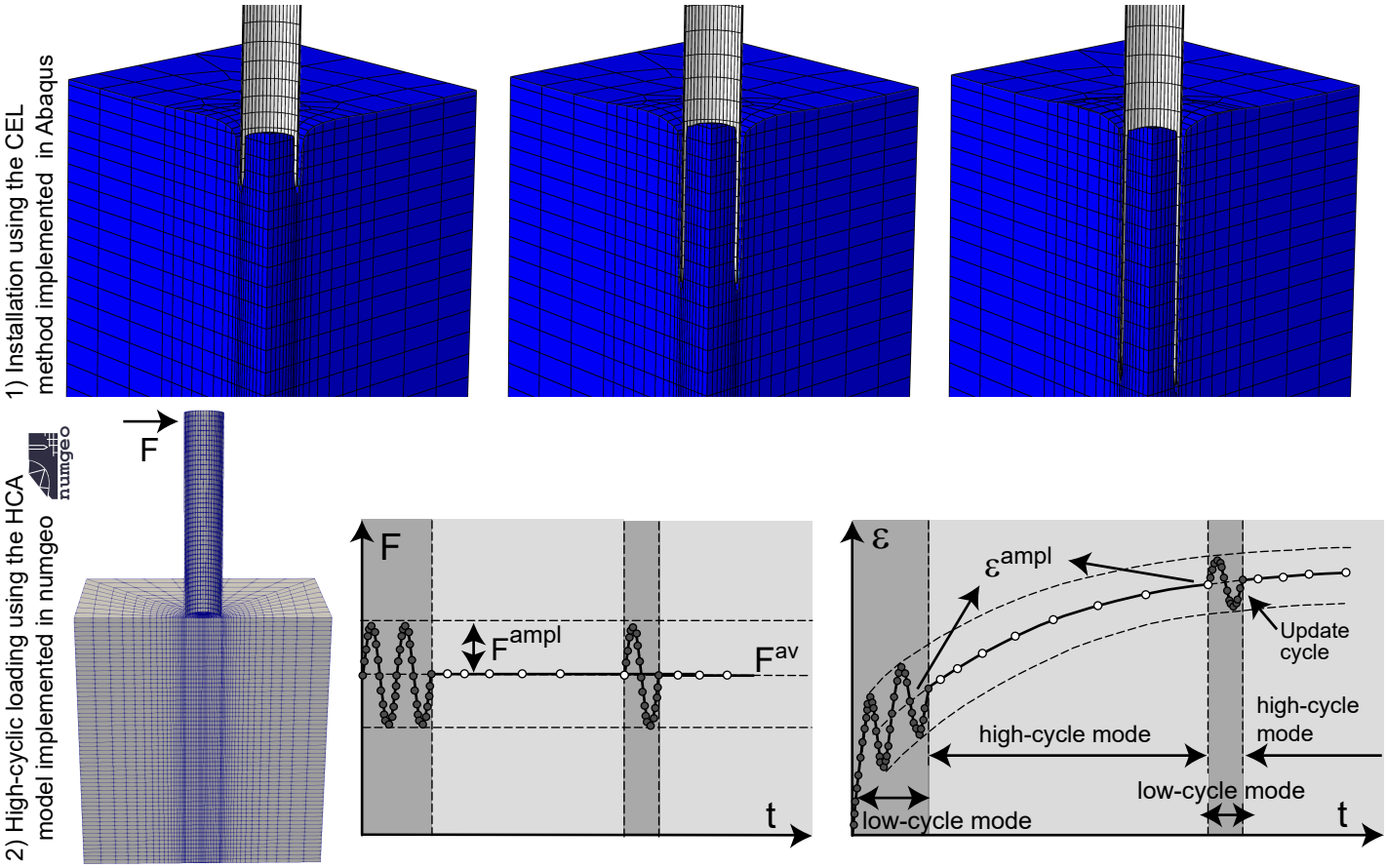

Figure 1: *Sequence of calculation steps: After the installation of the pile using the CEL method implemented in the commercial software Abaqus the high-cyclic loading is simulated by means of the HCA model implemented in the in-house finite element program numgeo using a combination of low-cycle and high-cycle calculation phases*

2 Models test by Leblanc et al.

The geometric specifications of the model tests are shown in Fig. 2. A copper pile with a diameter of $D = 0.08$ m, a wall thickness of $t = 0.002$ m and an embedment length of $L = 0.36$ m has been used. The pile has been driven into the soil using a plastic hammer. Dry yellow Leighton-Buzzard sand has been used. It was poured into the container from a low drop height in order to achieve a loose initial state. Tests with two different initial relative densities, $D_{r0} = 4\%$ and $D_{r0} = 38\%$, have been performed. The lateral loading of the pile has been applied in a height of $e = 0.43$ m above the ground surface. Different tests with varying amplitude and mean value of cyclic (harmonic) loading have been conducted. The number of applied cycles varied between $N = 8,000$ and $N = 20,000$ in the tests studied in the back-analysis. In the back-analysis, for both initial relative densities, the installation of the pile, a monotonic loading test to obtain the lateral capacity and at least one lateral cyclic loading test are considered. For the initial relative density of $D_{r0} = 38\%$ several cyclic loading tests with varying loading amplitude are simulated.

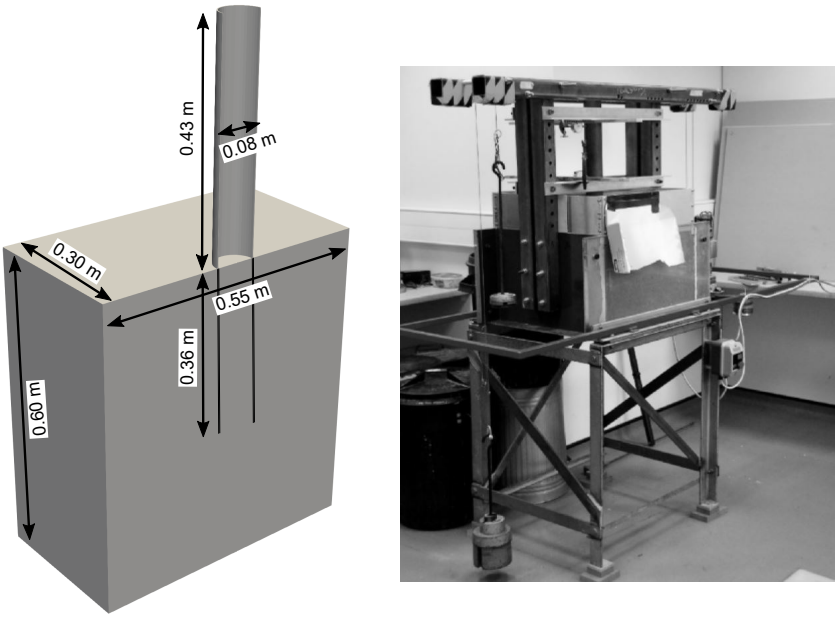

Figure 2: *Schematic sketch of the model tests and picture of the device (reprinted from (Leblanc et al., 2010))*

3 Constitutive models used for the back-analysis

Two different constitutive models are used for the back-analysis: the hypoplastic model proposed by von Wolffersdorff (Wolffersdorff, 1996) with the intergranular strain extension by Niemunis & Herle (Niemunis and Herle, 1997) (for the constitutive equations the interested reader is referred to A) and the HCA model of Niemunis et al. (Niemunis et al., 2005). The hypoplastic model with intergranular strain extension is used for the simulation of the installation process and the so-called *low-cycle* or *intrinsic* (formerly also denoted as *implicit*, not to be confused with implicit solution of differential equations) mode of the HCA model. For the simulation of cyclic loading with a large number of loading cycles ($N > 100$), the application of a conventional constitutive model is not expedient. This is due to the large calculation effort, an accumulation of numerical errors as millions of increments are necessary, and the inability of conventional constitutive models to adequately reproduce the cumulative effects during high-cyclic loading. Without enhancement by some kind of *memory-surface* (see for instance (Liu et al., 2019)), conventional models predict an almost linear increase in accumulated deformation with the number of applied load cycles, which contradicts the experimental observations of a decreasing rate of accumulation.

To overcome the aforementioned shortcomings, the HCA model works in a *high-cycle* or *extrinsic* (formerly also denoted as *explicit*) framework where only the trend of deformation is calculated, not the soil response during individual cycles (for the calculation strategy of the HCA model see the lower row in Fig. 1).

Following the simulation of two individual load cycles and the determination of the strain amplitude from the second cycle (the first cycle is *irregular* since the deformations in the first cycle often differ significantly from those in the subsequent cycles), the accumulation of permanent strain caused by the cyclic loading is treated analogously to the description of viscous creep by viscoplastic models for cohesive soils. Instead of the creep time t used in viscoplastic models, the number of load cycles N is the input for the HCA model. The HCA model calculates the accumulation of residual strain $\Delta\boldsymbol{\varepsilon}^{\mathrm{acc}} = \dot{\boldsymbol{\varepsilon}}^{\mathrm{acc}}\Delta N$ due to a package of ΔN cycles directly. A calculation of individual cycles is not necessary thus allowing to simulate an almost arbitrary number of cycles per calculation increment. The aforementioned restrictions regarding calculation effort or the accumulation of numerical error using conventional constitutive models

Function	Material constants
$f_{\text{ampl}} = \min\left\{\left(\frac{\varepsilon^{\text{ampl}}}{10^{-4}}\right)^{C_{\text{ampl}}}; 10^{C_{\text{ampl}}}\right\}$	C_{ampl}
$\dot{f}_N = \dot{f}_N^A + \dot{f}_N^B$	C_{N1}
$\dot{f}_N^A = C_{N1} C_{N2} \exp\left[-\frac{g^A}{C_{N1} f_{\text{ampl}}}\right]$	C_{N2}
$\dot{f}_N^B = C_{N1} C_{N3}$	C_{N3}
$f_e = \frac{(C_e - e)^2}{1+e} \frac{1+e_{\max}}{(C_e - e_{\max})^2}$	C_e
$f_p = \exp\left[-C_p \left(\frac{p^{\text{av}}}{100\ \text{kPa}} - 1\right)\right]$	C_p
$f_Y = \exp\left(C_Y\ \bar{Y}^{\text{av}}\right)$	C_Y
$f_\pi = 1$ for constant polarization, (Wichtmann, 2005)	

Table 1: Summary of the functions and material constants of the HCA model

are therefore circumvented. During the high-cycle phase the strain amplitude, which is an important input parameter of the HCA model, can be updated using so-called *update cycles* (see the lower row of Fig. 1).

The basic equation of the HCA model reads

$$\dot{\boldsymbol{\sigma}} = \mathsf{E} : (\dot{\boldsymbol{\varepsilon}} - \dot{\boldsymbol{\varepsilon}}^{\text{acc}} - \dot{\boldsymbol{\varepsilon}}^{\text{pl}}) \tag{1}$$

with the stress rate $\dot{\boldsymbol{\sigma}}$ of the effective Cauchy stress $\boldsymbol{\sigma}$, the strain rate $\dot{\boldsymbol{\varepsilon}}$, the strain accumulation rate $\dot{\boldsymbol{\varepsilon}}^{\text{acc}}$, a plastic strain rate $\dot{\boldsymbol{\varepsilon}}^{\text{pl}}$ (necessary only if the stress touches the Matsuoka-Nakai failure locus) and the pressure-dependent elastic stiffness E (note that the geotechnial sign convention is used for stress and strain). In Eq. (1) the dot over a variable denotes the derivative with respect to the number of cycles N (instead of time t).

The strain accumulation rate $\dot{\boldsymbol{\varepsilon}}^{\text{acc}}$ in Eq. (1) is calculated by the following multiplicative approach

$$\dot{\boldsymbol{\varepsilon}}^{\text{acc}} = \dot{\varepsilon}^{\text{acc}}\ \mathbf{m} \tag{2}$$

where $\mathbf{m} = \dot{\boldsymbol{\varepsilon}}^{\text{acc}} / \|\dot{\boldsymbol{\varepsilon}}^{\text{acc}}\| = (\dot{\boldsymbol{\varepsilon}}^{\text{acc}})^{\rightarrow}$ is the *direction* of strain accumulation and $\dot{\varepsilon}^{\text{acc}} = \|\dot{\boldsymbol{\varepsilon}}^{\text{acc}}\|$ is the *intensity* of strain accumulation. The flow rule of the Modified Cam Clay (MCC) model is applied for $\mathbf{m}$, which has been found suitable from extensive laboratory testing (Wichtmann, 2005; Wichtmann et al., 2006).

The scalar strain accumulation rate $\dot{\varepsilon}^{\text{acc}}$ in Eq. (2) is calculated as a product of six functions, each considering a different influencing factor:

$$\dot{\varepsilon}^{\text{acc}} = f_{\text{ampl}}\ \dot{f}_N\ f_e\ f_p\ f_Y\ f_\pi \tag{3}$$

The factors take into account the influence of the strain amplitude $\varepsilon^{\text{ampl}}$ (function f_{ampl}), the cyclic preloading ($\dot{f}_N$, using the preloading variable g^A which weights the number N of applied cycles with the strain amplitude $\varepsilon^{\text{ampl}}$ of these cycles), the void ratio e (f_e), the average mean pressure p^{av} (f_p), the normalized average stress ratio $\bar{Y}^{\text{av}}$ (f_Y, $\bar{Y}^{\text{av}} = 0$ at isotropic stresses, $\bar{Y}^{\text{av}} = 1$ at critical stress ratio) and the effect of polarization changes ($f_\pi = 1$ for a constant direction of cyclic loading).

The equations given in Table 1 have been developed and verified by a comprehensive experimental study reported in (Wichtmann, 2005; Wichtmann et al., 2005; Wichtmann et al., 2006; Wichtmann et

al., 2007a; Wichtmann et al., 2010a; Wichtmann et al., 2007b; Wichtmann et al., 2013; Wichtmann and Triantafyllidis, 2015; Wichtmann et al., 2014). The parameters of the HCA model can be determined from experiments (Wichtmann et al., 2010b; Wichtmann et al., 2015) or estimated based on granulometry or simple index quantities (Wichtmann et al., 2009; Wichtmann et al., 2015). The determination of parameters for the HCA model based on the procedure described in (Wichtmann et al., 2015) is presented for the yellow Leighton-Buzzard sand in Section 4.2.

4 Parameter calibration of the constitutive models

An extensive laboratory testing program has been conducted on yellow Leighton-Buzzard sand in order to calibrate the parameters of the hypoplastic model with intergranular strain extension and the parameters of the HCA model. Sieve analyses have confirmed that the charge of yellow Leighton-Buzzard sand used in the laboratory tests was similar to the one applied in the model tests of Leblanc et al (Leblanc et al., 2010).

Several oedometric compression tests, drained monotonic triaxial tests with low stress level, undrained cyclic triaxial tests and drained high-cyclic triaxial tests were conducted. In the oedometric compression and monotonic triaxial tests different initial densities have been considered in order to secure that the material behaviour is correctly grasped for a wide range of densities from very loose to dense states. This is important in the present case as the pile driving process leads to strongly inhomogeneous distributions of relative density (and stresses), with D_r values comprising the whole range between 0 % and 100 %. For the cyclic tests, as they are more laborious, only one undrained cyclic and one drained high-cyclic test have been performed.

The element test program *Incremental Driver* by Niemunis (Niemunis, 2008) has been used for the simulation of the laboratory tests and the optimization of the material constants for the hypoplastic model with intergranular strain extension. The simulations of the laboratory tests were repeated until the optimum set of parameters was found.

4.1 Parameters of the hypoplastic model with intergranular strain extension

The critical friction angle has been determined based on five cone deposition tests which gave a mean value of $\varphi_c = 33.3°$. The minimum and maximum void ratios have been evaluated by standard tests. Using $e_{c0} = e_{\max}$, $e_{d0} = e_{\min}$ and $e_{i0} = 1.15 \cdot e_{\max}$ as proposed by (Herle, 1997), the first four parameters of the hypoplastic model are obtained (see Table 2).

The hypoplastic parameters h_s, n and β are obtained from oedometric compression tests. Fig. 3 displays the results of oedometric compression tests on yellow Leighton-Buzzard sand with varying initial density (dashed lines). The results of corresponding element test simulations using the hypoplastic model with the parameters given in Table 2 are added as the solid lines. A satisfying accordance for both initially loose and dense samples is achieved.

The parameter α is calibrated based on drained monotonic triaxial tests. Several such tests with varying initial density and two different initial mean effective stresses p, namely 20 kPa and 50 kPa, have been performed. The low level of stress is chosen to represent the stress level in the model tests as close as possible (however, as the model tests had approximately a mean effective stress of $p = 3$ kPa at the half height of the device, the stress is still considerably higher in the triaxial tests). The curves of deviatoric stress q and volumetric strain ε_{vol} versus axial strain ε_1 obtained from the experiments and the simulations using hypoplasticity with the parameters in Table 2 are compared for $p = 20$ kPa in Fig. 4

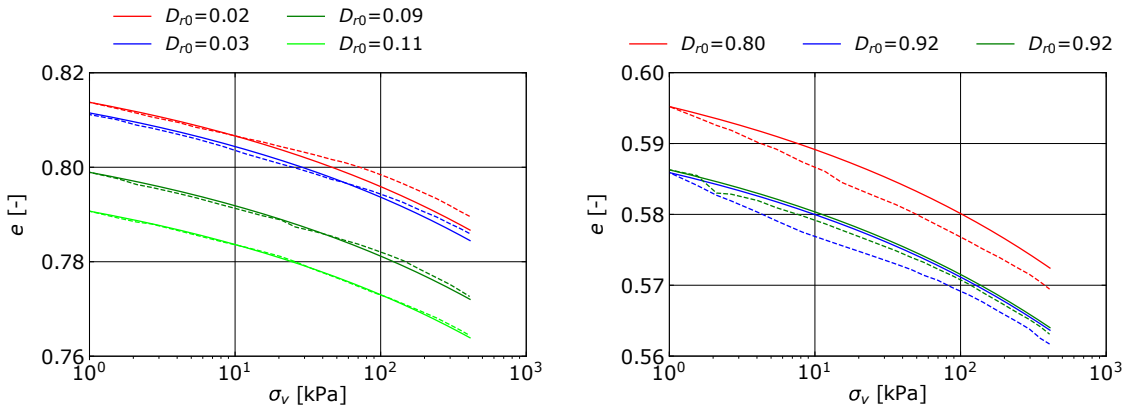

Figure 3: *Results of oedometric compression tests for initially loose and initially dense yellow Leighton-Buzzard sand (dashed lines). The solid lines represent the simulations using the hypoplastic model with the parameters given in Table 2.*

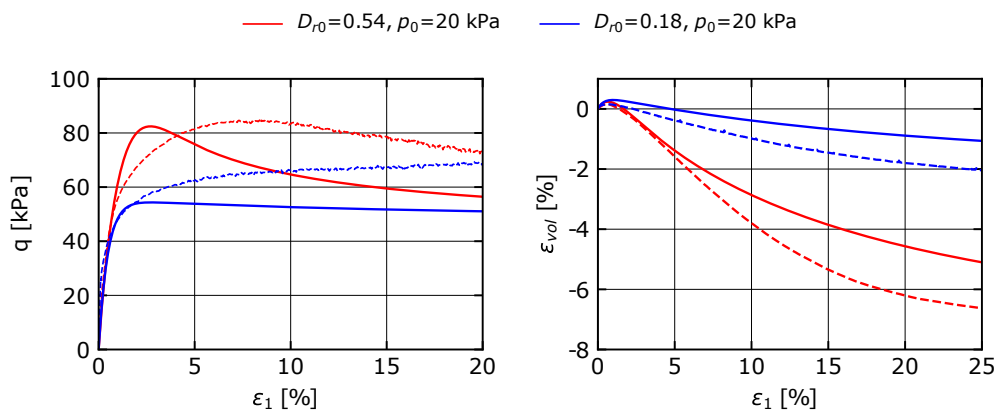

Figure 4: *Results of drained monotonic triaxial tests with an initial mean effective stress of $p = 20$ kPa and varying initial density. The dashed lines represent the experiments, while the solid lines represent the simulations using hypoplasticity with the parameters given in Table 2.*

φ_c [-]	e_{i0} [-]	e_{c0} [-]	e_{d0} [-]	h_s [kPa]	n [-]	α [-]	β [-]
33.3°	0.930	0.809	0.507	$1.9 \cdot 10^7$	0.191	0.223	-1.3

R [-]	m_R [-]	m_T [-]	β_R [-]	χ [-]
10^{-4}	4	2	0.1	4.6

Table 2: Parameters of hypoplasticity with intergranular strain extension for yellow Leighton-Buzzard sand

and for $p = 50$ kPa in Fig. 5. For all four tests, the measured sand response is generally reproduced quite well in the simulations. However, the residual deviatoric stress is underestimated by the simulations. This is stronger in case of the tests performed at $p = 20$ kPa. In addition, dilatancy is underestimated for all tests.

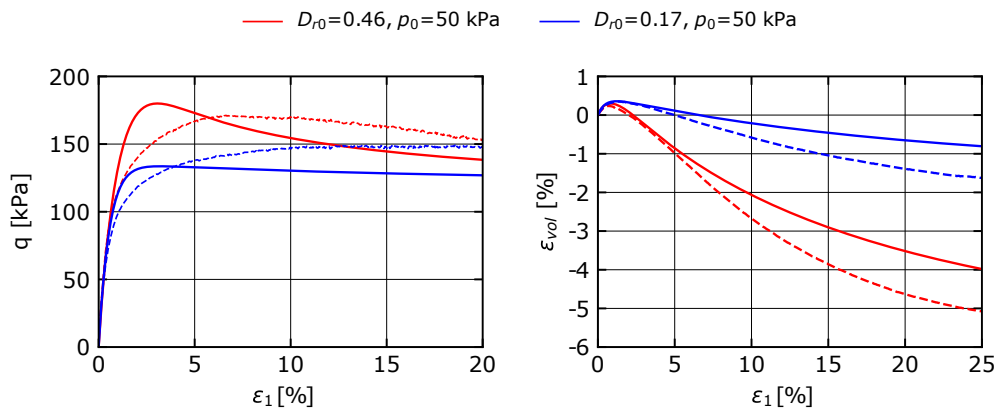

Figure 5: *Results of drained monotonic triaxial tests with an initial mean effective stress of $p = 50$ kPa and varying initial density. The dashed lines represent the experiments, while the solid lines represent the simulations using hypoplasticity with the parameters given in Table 2*

In order to calibrate the parameters of the intergranular strain, the data of the undrained cyclic triaxial test with stress control is used. Once more, a low stress level of $p = 50$ kPa has been chosen as initial stress state in this test. The soil had an initial relative density of 71 %. The deviatoric stress q versus mean effective stress p and versus axial strain ε_1, respectively, is given in the upper diagrams of Fig. 6. The lower diagrams display the accumulated excess pore water pressure and the axial strain amplitude $\varepsilon_1^{\text{ampl}}$ as functions of the number of cycles N. The development of both the accumulated excess pore water pressure and the axial strain amplitude are well reproduced by the numerical simulation with the parameters in Table 2 before cyclic mobility occurs. The correct representation of cyclic mobility by the constitutive model is of minor importance in the present case, as the model tests have been performed on dry sand. The most important aspect in view of the model tests is the strain amplitude during the cycles. The data in Fig. 6 confirms that the small strain amplitudes before the cyclic mobility phase are captured very well with the chosen set of parameters.

Note that all tests (oedometric, monotonic and cyclic triaxial tests) have been simulated with the same set of parameters presented in Table 2.

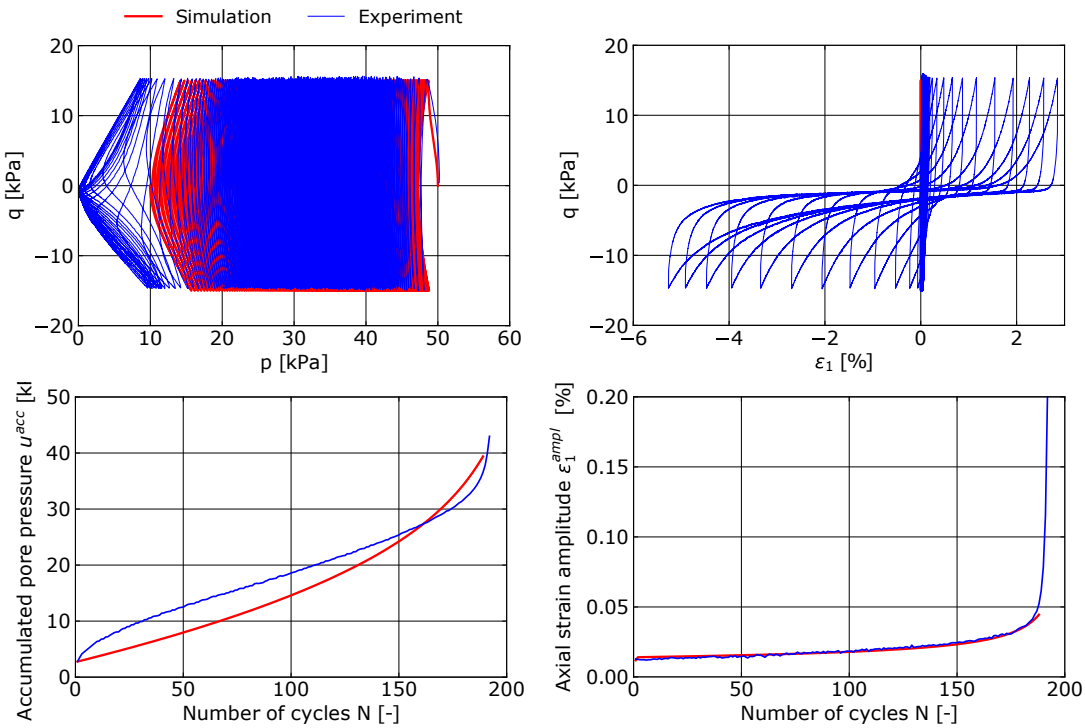

Figure 6: *Results of an undrained cyclic triaxial test performed on yellow Leighton-Buzzard with an initial mean effective stress of $p = 50$ kPa, an initial relative density of 72 % and a deviatoric stress amplitude of $q^{ampl} = 15$ kPa. The upper plots display the effective stress path in the p-q plane and the deviatoric stress q versus axial strain ε_1 relationship. The lower plots display the accumulated excess pore water pressure and the axial strain amplitude as functions of the number of cycles N. The test data is shown in blue colour, while the simulation using the parameters given in Table 2 is displayed in red colour.*

C_{ampl}	C_e	C_p	C_Y	C_{N1} $[10^{-4}]$	C_{N2}	C_{N3} $[10^{-5}]$
1.7	0.482	0.38	2.69	3.1	0.063	3.7

Table 3: Parameters of the HCA model for yellow Leighton-Buzzard sand

4.2 Parameters of the high-cycle accumulation model

The complete determination of the material constants of the HCA model requires at least eleven drained high-cyclic triaxial tests with varying strain amplitudes, initial relative densities, average mean stresses and average stress ratios. However, based on approximately 150 drained cyclic triaxial tests, a simplified calibration procedure has been proposed in (Wichtmann et al., 2015). Even though all necessary parameters can be estimated based on the mean grain size d_{50}, the uniformity coefficient C_u and minimum void ratio $e_{\min}$, it is recommended to conduct at least one drained high-cyclic triaxial test in order to calibrate the parameters C_{N1}, C_{N2} and C_{N3}, which describe the development of accumulated strain with increasing number of cycles, that means consider the cyclic preloading. Following the procedure described in (Wichtmann et al., 2015), the parameters C_{ampl}, C_e, C_p and C_Y can be estimated as follows:

$$C_{\text{ampl}} = 1.7 \tag{4}$$

$$C_e = 0.95 \cdot e_{\min} \tag{5}$$

$$C_p = 0.41 \cdot [1 - 0.34\ (d_{50}[\text{mm}] - 0.6)] \tag{6}$$

$$C_Y = 2.60 \cdot [1 + 0.12\ \ln(d_{50}[\text{mm}]/0.6)]. \tag{7}$$

For yellow Leighton-Buzzard sand the parameters obtained from these equations are listed in Table 3.

Fig. 7 displays the result of a drained high-cyclic triaxial test on Leighton-Buzzard sand used for the calibration of C_{N1}, C_{N2} and C_{N3}. The sample had an initial relative density of 54 %, an average mean effective stress of $p^{\text{av}} = 200$ kPa, an average stress ratio of $\eta^{\text{av}} = q^{\text{av}}/p^{\text{av}} = 0.75$ and a cyclic amplitude of 60 kPa. The measured accumulated strain is divided by the factors f_{ampl}, f_e, f_p and f_Y and shown as a function of the number of cycles. These functions are calculated using the equations provided in Table 1 and the material constants given in Table 3. The necessary soil state variables for the calculation of the factors (the strain amplitude $\varepsilon^{\text{ampl}}$, the average mean stress p^{av}, the average void ratio e^{av} and normalized average stress ratio $\bar{Y}^{\text{av}}$) are known from the test. The constants C_{N1}, C_{N2} and C_{N3} are then obtained by curve fitting using

$$f_N = C_{N1}[\ln(1 + C_{N2}N) + C_{N3}N]. \tag{8}$$

The curve fit is displayed in Fig. 7. The parameters obtained are $C_{N1} = 3.1 \cdot 10^{-4}$, $C_{N2} = 0.063$ and $C_{N3} = 3.7 \cdot 10^{-5}$.

5 Simulation of the installation process

Due to the large deformations occurring during the installation process, special numerical treatment is necessary. Pile driving has been simulated utilizing various numerical approaches which include simulations using a fully Lagrangian description of the soil (reported e.g. in (Chrisopoulos and Vogelsang, 2019; Grandas-Tavera et al., 2019; Staubach and Machacek, 2019)), an Eulerian description (see e.g. (Qiu et al., 2011; Hamann et al., 2015; Wang et al., 2015; Nagula and Grabe, 2020; Staubach et al., 2020c; Staubach et al., 2020b; Staubach et al., 2020a)), an Arbitrary Lagrangian-Eulerian (ALE) approach (reported e.g. in (Daryaei et al., 2020; Yang et al., 2020)) or the Material-Point-Method (e.g. (Phuong

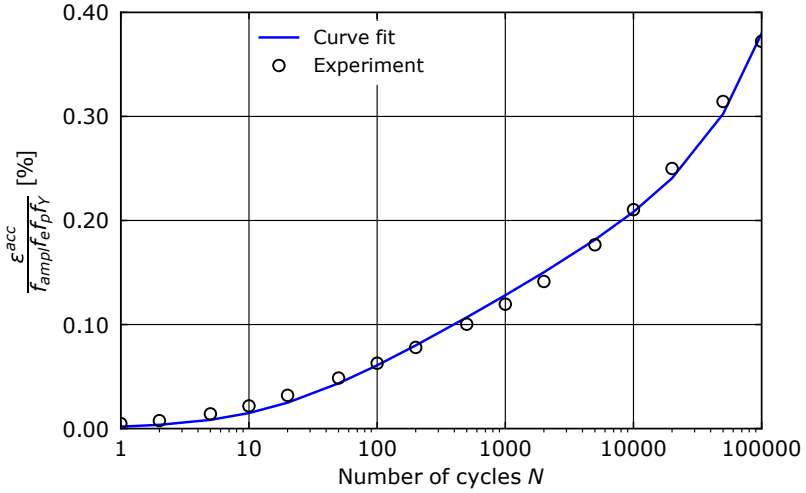

Figure 7: *Development of accumulated strain ε^{acc} divided by the factors f_{ampl}, f_e, f_p and f_Y with increasing number of cycles obtained from a drained high-cyclic triaxial test on yellow Leighton-Buzzard sand. The experimental data (circular symbols) is confronted with a curve-fit using Eq. (8) (solid curve)*

et al., 2014; Galavi et al., 2019)). For the simulation of the installation of open-profile piles, a fully Lagrangian approach is not suitable. Therefore, an Eulerian description is used for the soil in the present study which has been applied by the authors for the simulation of the installation of open-profile piles in (Staubach et al., 2020c; Staubach et al., 2020b; Staubach et al., 2020a) as well. The back-analysis of vibratory pile driving model tests in water-saturated sand reported in (Staubach et al., 2020a) showed a very good performance of this approach.

In an Eulerian analysis, the mesh is fixed in space and the material transport is predicted. This is advantageous for the modelling of large deformations since no mesh distortion takes place. The pile, as an almost rigid body with merely small intrinsic deformation, is modelled under the Lagrangian framework. Using the Coupled-Eulerian-Lagrangian (CEL) method implemented in the commercial software Abaqus, the two parts (soil and pile) can interact with each other by special contact conditions. For more information regarding the CEL method, the interested reader is referred to (Benson, 1992; Benson and Okazawa, 2004) for the theoretical background and e.g. (Staubach et al., 2020c; Staubach et al., 2020b; Staubach et al., 2020a) for the application of the CEL method to geotechnical boundary value problems.

5.1 Numerical model for the pile driving process

The numerical model used for the simulation of installation is displayed in Fig. 8 a). The red volume is initially free of material but could be filled if the soil heaves during the driving process. The blue volume is initially fully filled by material. The material-filled volume has the same dimensions as the sand container used in the experiment displayed in Fig. 2. Exploiting the symmetry of the boundary value problem, a quarter model is considered for the simulation of the installation process to reduce the computational costs. The element size in the horizontal direction below the pile tip is identical to the thickness of the pile (0.002 m). The size increases progressively with radial distance to the pile. In vertical direction the element size is 0.006 m directly at the ground surface and increases to 0.015 m at the final embedment depth of the pile.

The initial relative densities are set identical to the values in the model tests, that means 4 % and 38 %, respectively. The hypoplastic model with intergranular strain extension and the parameters listed in Table 2 are used. Despite considering dry sand, the mean effective stress in the soil reduces strongly in

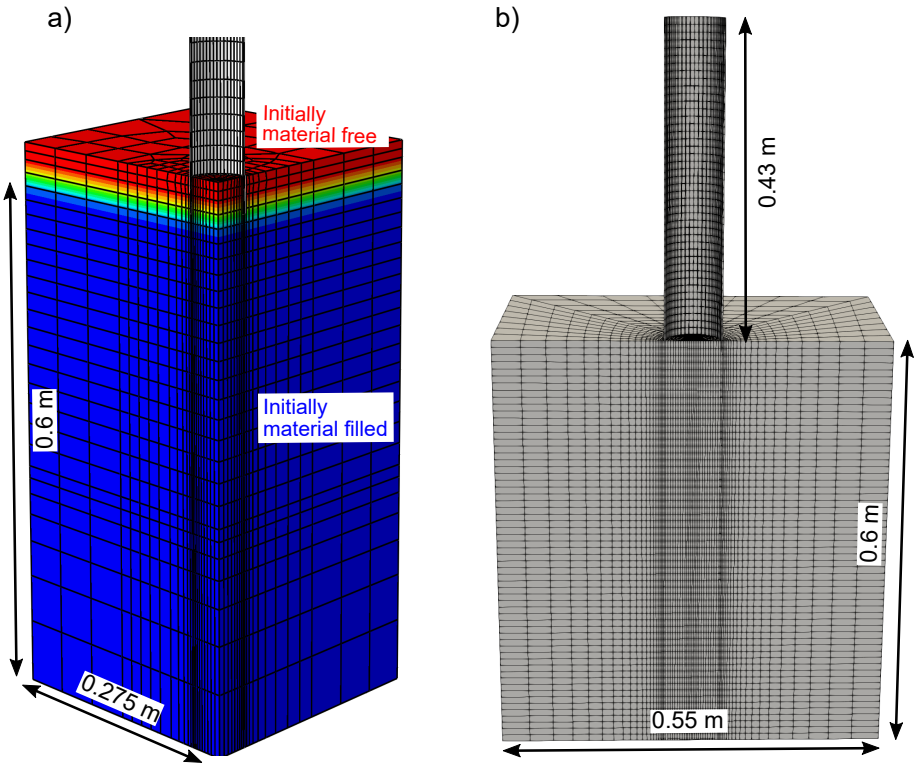

Figure 8: *Numerical models for the simulation of the installation process (a) and for the high-cyclic loading (b). The initial volume fraction is displayed for the CEL model. The blue volume indicates initially fully material-filled elements while the red volume indicates initially material-free elements.*

some elements during the driving process. If the mean effective stress approaches zero, the hypoplastic model yields a zero or even non-physical stiffness. Therefore, a correction for small mean effective stresses ($p < 0.01$ kPa) is used. This correction is then followed by a correction of stress states located outside the Matsuoka-Nakai failure locus. This approach was proposed in (Osinov et al., 2016) and has also been used in (Staubach and Machacek, 2019; Machacek et al., 2018) for the simulation of vibratory pile driving in water-saturated soil and liquefaction during earthquake loading, respectively.

Friction between pile and soil is considered using a Coulomb friction model. The wall friction angle is assumed to be 2/3 of the critical friction angle. Effects resulting from grain crushing in the vicinity of the pile or abrasion are not taken into account.

In the model tests performed by Leblanc et al. the pile has been driven into the soil with a plastic hammer. Even though the number of strokes needed to drive the pile to its final embedment depth is known, the specification of the hammer and the drop height is unknown. Since the influence of different installation techniques (jacking vs. impact driving) proved insignificant for the lateral cyclic response of the pile once installed (see (Staubach et al., 2020c; Staubach et al., 2020b)), the pile is jacked into the soil in the simulation assuming that the change in the soil surrounding the pile is similar to impact driving. Note that in an experimental study reported in (Fan et al., 2019; Fan, 2020), impact-driven piles were found to have higher resistance to subsequent monotonic lateral loading compared to jacked piles. In order to investigate how large the influence of the method of installation is in the present case, additional simulations considering impact driving are presented in B. Even though the impact-driven pile exhibits slightly larger resistance to lateral monotonic loading compared to the jacked pile, the relative difference between the two installation techniques is small. Therefore, the simulation of pile installation using jacking appears to be justified in the present case.

A jacking speed of 0.06 m/s is assumed in the simulations. Inertia effects are considered and an explicit

time integration scheme is used.

5.2 Results of the pile driving process

The development of relative density during the driving process for the simulation of the test with an initial relative density of $D_{r0} = 38$ % is depicted in Fig. 9. The spatial field is displayed for different stages of the simulation and the current depth of embedment t is given. The soil near the top surface heaves and reaches a very loose state. In the vicinity of the pile tip the soil tends to densify considerably. This is more pronounced inside of the pile compared to the outside. In addition, the densified zone is restricted to soil close to the pile shaft. With increasing distance to the outer shaft of the pile, the relative density decreases and reaches values lower than the initial relative density.

The development of relative density shown in Fig. 9 is comparable to the results of simulations of impact driving or jacking of real-scale piles reported in (Staubach et al., 2020c; Staubach et al., 2020b), in case of simulations with a similar initial relative density. The qualitative change in relative density caused by the installation process is thus comparable for small-scale model tests and real-scale problems.

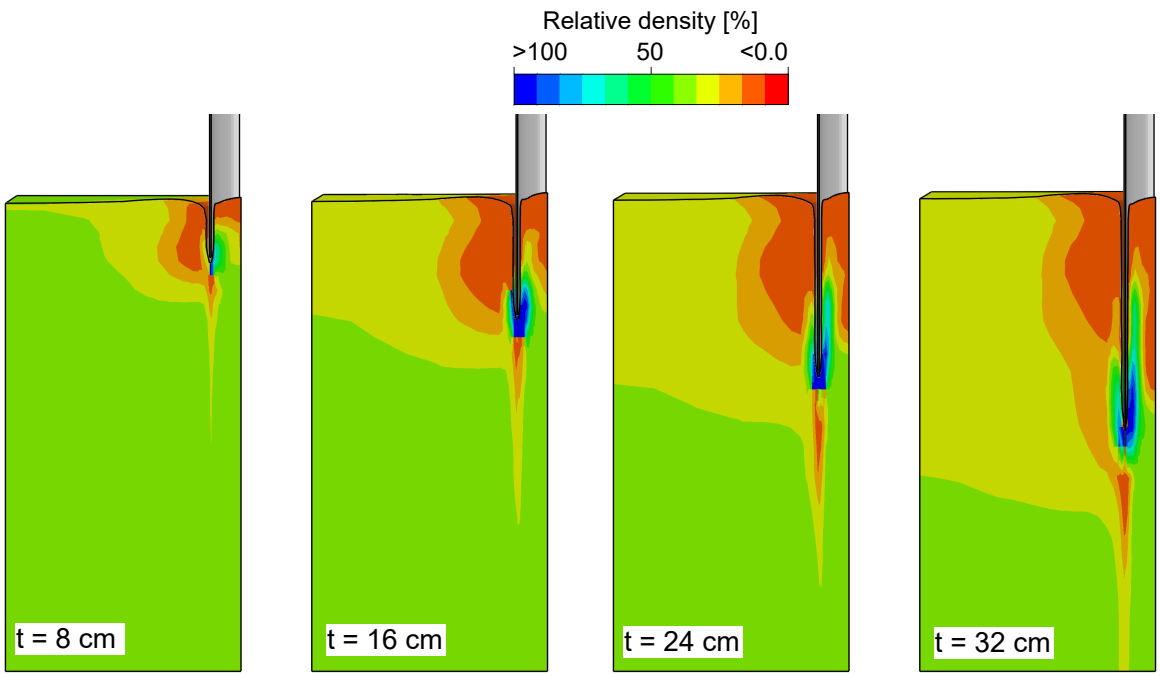

Figure 9: *Development of relative density during the driving process for the test with an initial relative density of $D_{r0} = 38$ %. The embedment depth t is given for each stage of the installation process.*

The change of mean effective stress during the driving process is shown in Fig. 10. A strong increase in pressure with values above 100 kPa is observed below the pile tip. During the driving process, the area of high pressures increases and eventually reaches the fixed bottom of the model. While the stress increases below the pile tip, a strong decrease alongside the (outer) pile shaft is observed. This effect has also been observed for the simulation of real-scale pile installation (Staubach et al., 2020c; Staubach et al., 2020b) as well as in experimental studies of displacement pile installation (see e.g. (White and Bolton, 2004; Yang et al., 2010; Gourvenec and Randolph, 2011)).

The results of the pile installation for the test with an initial relative density of $D_{r0} = 4$ % are presented and discussed in C. A strong compaction and stress increase in the vicinity of the pile tip is observed similar to the test with an initial relative density of $D_{r0} = 38$ %.

For the simulation of the lateral loading of the pile presented in the following section, an implicit Lagrangian simulation is performed since the high-cycle phase with the HCA model can not be simulated

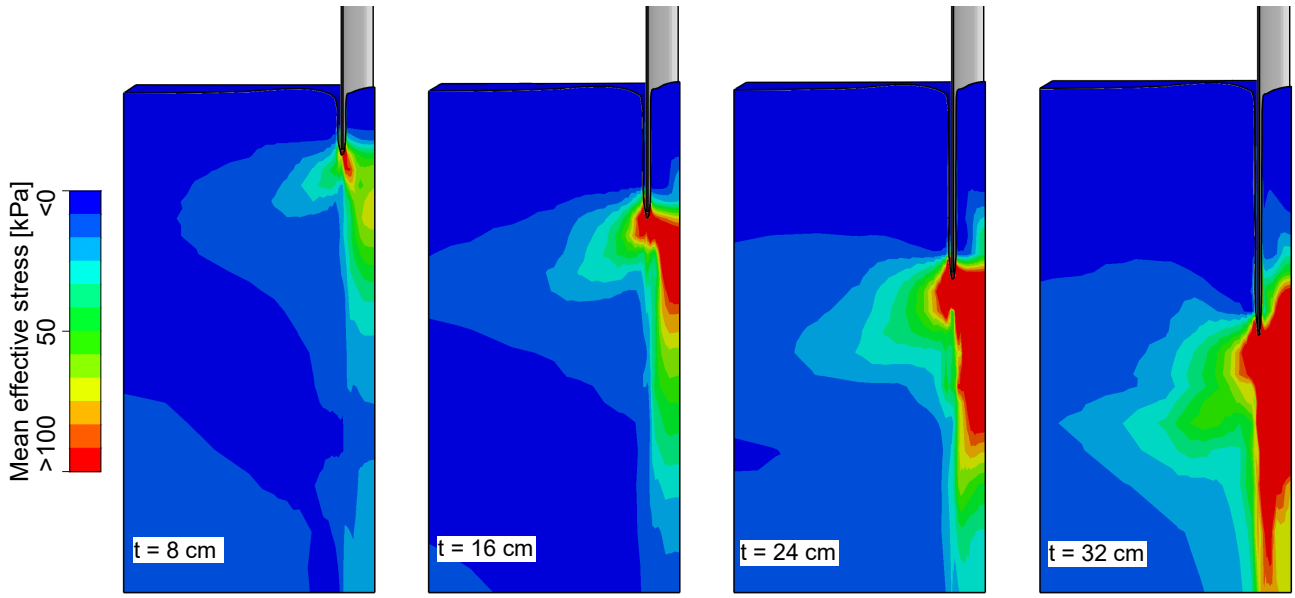

Figure 10: *Development of mean effective stress during the driving process for the test with an initial relative density of* $D_{r0} = 38$ *%*

using an explicit time integration scheme. Therefore, the state of the soil resulting from the installation is transferred from the CEL model to a model with Lagrangian elements as described in the following.

6 Lateral loading of the pile after the installation

6.1 Numerical model

The simulations of the lateral loading of the pile are performed with the new finite element code `numgeo`[1]. The hypoplastic model with intergranular strain extension and the HCA model are implemented in `numgeo`.

Linearly interpolated 3D Lagrangian elements with reduced integration are used for the soil. Elements with reduced integration are beneficial in simulations with the HCA model as artificial self-stresses are avoided (Niemunis and Melikayeva, 2015). An hourglass stiffness of 100 kPa has been used for all calculations to suppress any hourglass deformation modes. Simulations with much lower (20 kPa) or much higher values (300 kPa) for the hourglass stiffness did not reveal any differences in terms of pile rotation. The model including the mesh is displayed in Fig 8b. Due to the unidirectional lateral loading it is sufficient to model only one half of the model test making use of the symmetry. The finite-element model is discretised using approximately 60,000 nodes and 50,000 elements. The pile is modelled deformable and the material properties of copper are used.

The contact between pile and soil is discretised using a surface-to-surface method and the contact constraints are enforced by the penalty method. The penalty factor in normal direction is calculated based on the material stiffness of the continuum element closest to the contact point. By default, the penalty factor is thirty times the trace of the stiffness. This ensures that the penetration of the soil into the pile is minimal and the normal contact constraint is enforced properly. A stiffness dependent penalty

[1] `numgeo` (see the PhD thesis of J. Machaček (Machaček, 2020) and `www.numgeo.de`) is an inhouse finite-element program, developed by the first two authors for the solution of non-linear, coupled (dynamic) geotechnical boundary value problems. A release of a free version is planned for 2021. All program features required for the simulations presented herein will be available in this release.

factor is superior in terms of convergence to a spatially constant value in the present simulations due to the change of soil stiffness with respect to the pile embedment depth (i.e. highest stiffness at the base, especially for the simulation incorporating the installation process).

Friction is considered using a Coulomb model with a wall friction angle of 2/3 of the critical friction angle of the soil. A stabilizing pressure of 0.05 kPa has been applied on the ground surface in order to avoid zero pressure in the soil close to the surface. This additional surface pressure does not influence the results of the simulations, which was proven by simulations without any surface pressure. Simulations with a higher value of surface pressure, e.g. 0.5 kPa, show a considerable influence and lead to a decreased pile rotation when the pile is subjected to lateral loading.

Due to the large deformations in the monotonic tests and in the cyclic tests with large amplitudes, a geometrically non-linear calculation is performed. The Zaremba-Jaumann stress rate is used in order to ensure an objective stress rate.

Preliminary simulations incorporating update cycles, used for the determination of an updated strain amplitude in the high-cycle phase of the HCA model, showed no significant differences to simulations without update cycles. This is in accordance with the observations documented in (Staubach et al., 2020c).

The state variables of the soil after the installation are transferred from the integration points in the CEL model to the closest integration points in the Lagrangian model. The stress, void ratio and the intergranular strain tensor are transferred. The deformation of the soil caused by the installation process is not considered in the Lagrangian model as the material movements are judged insignificant compared to the influence of the change in state variables. In a distance of 0.005 m around the pile the soil has settled by approximately 0.008 m ($= 0.1 \cdot D$). In greater distance to the pile as well as inside of the pile a maximum heave of approximately 0.004 m ($= 0.05 \cdot D$) is observed.

It is important to note that the stress state resulting from the installation depicted in Fig. 10 is not in static equilibrium since considerable inertia forces are still present at the end of the CEL simulation (no additional resting period after the installation has been considered). In addition, the mapping procedure also adds inaccuracies leading to further unbalance forces. Thus, the stress will change slightly once the soil state is imported in the Lagrangian model and the soil is free to move. An additional calculation step is included to bring the model in static equilibrium prior to the lateral loading of the pile.

6.2 Monotonic loading to failure

Prior to the cyclic tests, a monotonic loading test has been performed by Leblanc et al. in order to determine the static moment capacity $\tilde{M}_R$. The non-dimensional moment $\tilde{M}$ is defined by (Leblanc et al., 2010)

$$\tilde{M} = \frac{M}{L^3 D \gamma} \tag{9}$$

where M is the applied moment, L and D are the embedded length and the diameter of the pile, respectively, and γ is the specific unit weight of the (dry) soil. The non-dimensional rotation $\tilde{\theta}$ is defined by (Leblanc et al., 2010)

$$\tilde{\theta} = \theta \sqrt{\frac{p_a}{L\gamma}}. \tag{10}$$

Therein θ is the rotation of the pile and $p_a \approx 100$ kPa is the atmospheric pressure.

The non-dimensional moment versus the non-dimensional rotation for the experiment and the sim-

ulations with and without consideration of the installation is given in Fig. 11, for the initial relative densities of $D_{r0} = 38$ % and $D_{r0} = 4$ %, respectively. Leblanc et al. defined the ultimate-limit-state (ULS) rotation of the pile to be $\tilde{\theta} = 0.0698$ rad $= 4°$, corresponding to a static non-dimensional moment capacity of $\tilde{M}_R \approx 1.24$ for $D_{r0} = 38$ % and $\tilde{M}_R \approx 0.6$ for $D_{r0} = 4$ %.

It can be seen that the simulations without consideration of the installation process strongly underestimate the resistance of the pile for both initial densities. This is especially pronounced during the first half of the loading process. Thus, the initial stiffness of the pile is predicted too low compared to the experiment. For the initial relative density of $D_{r0} = 38$ % the non-dimensional moment at the ULS rotation $\tilde{\theta} = 0.0698$ rad is approximately 25 % lower than the corresponding measured value. The results of the simulation considering the installation process fit better to the experimental data even though the pile resistance at the end of the test is still slightly underestimated. In case of the test with an initial relative density of $D_{r0} = 4$ % the initial stiffness is underestimated by both simulation types but the final resistance is reproduced quite well by the simulation taking into account the installation process.

Based on the large differences between the simulations, it is concluded that the installation-induced soil changes considerably influence the pile response to monotonic lateral loading. However, assuming wished-in-place conditions is a conservative assumption in terms of pile displacement. The stiffness and hence the natural frequency of the pile is underestimated, however. Similar conclusions were drawn for the simulation of real-scale piles reported in (Staubach et al., 2020c).

As has been outlined in the introduction, the study reported in (Fan et al., 2019) has investigated the influence of the pile installation on its response to lateral loading by performing the installation process at 1g and 100g, respectively. The relative increase in the lateral soil resistance due to the installation process observed in (Fan et al., 2019) is qualitatively and quantitatively similar to the differences found in the numerical results presented in Fig. 11.

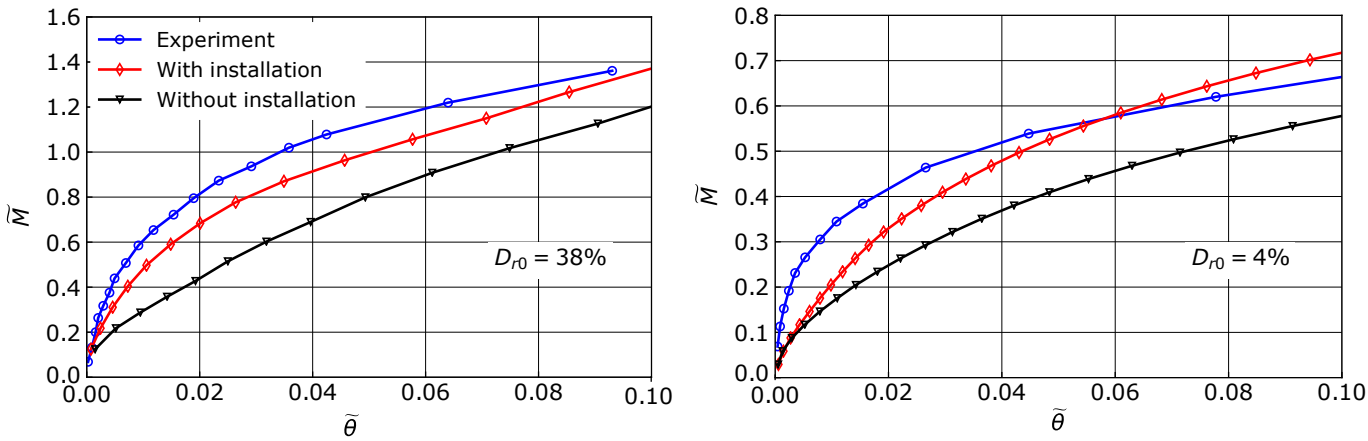

Figure 11: *Results of the monotonic loading tests: Comparison of the curves of non-dimensional moment $\tilde{M}$ versus non-dimensional rotation $\tilde{\theta}$ measured in the experiment and obtained from the simulations with and without consideration of the installation process, respectively. The diagram on the left-hand side refers to an initial relative density of $D_{r0} = 38$ %, that on the right-hand side to $D_{r0} = 4$ %.*

6.3 Cyclic loading

Based on the static moment capacity M_R obtained from the tests with monotonic loading, two parameters ζ_b and ζ_c are used to characterise the cyclic loading (Leblanc et al., 2010)

$$\zeta_b = \frac{M_{\max}}{M_R} \quad \text{and} \quad \zeta_c = \frac{M_{\min}}{M_{\max}}. \tag{11}$$

$M_{\max}$ and $M_{\min}$ are the maximum and minimum moments in a sinusoidal load cycle. The static moment capacities M_R measured in the model tests have been used for the calculation of the load amplitudes in the simulations.

The results in terms of the change of rotation $\Delta\theta$ at the pile head with respect to the first load cycle divided by the static rotation θ_s versus the number of cycles N for test No. 17 ($D_{r0} = 38$ %, $\zeta_b = 0.4$ and $\zeta_c = 0$) are given in Fig. 12. The values measured in the model tests and those obtained from the simulations with and without installation, respectively, are compared. Note that in the experiment θ_s has been determined at the point of maximum load application in the first cycle and $\Delta\theta$ has been also measured with respect to the point of maximum load application. In the simulations, however, θ_s is the rotation after the first cycle and $\Delta\theta$ is the change in rotation with respect to the rotation at the end of the first cycle. This is because the HCA model calculates the trend of deformation under the average loads, and $\Delta\theta$ can thus not be quantified at the point of maximum load application during a cycle. However, this doesn't influence the comparison between experiment and simulation as long as the rotation amplitude in an individual cycle does not change considerably during the long-term loading, which is generally not the case. Note that θ_s in the simulations is slightly higher than in the experiments as has been shown by the simulations of the monotonic tests displayed in Fig. 11. These differences are more pronounced in case of the simulation without considering installation. Therefore, the ratio $\Delta\theta/\theta_s$ may be too small in the simulations compared to the experiments due to a weaker monotonic response of the pile in the simulations, and not because the accumulation is too low in the HCA phase.

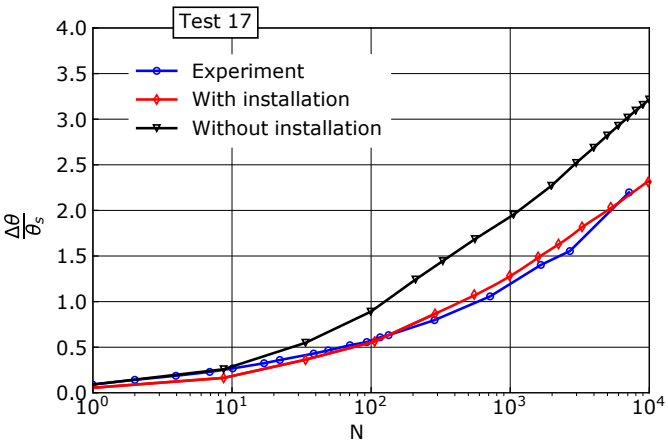

Figure 12: *Change of rotation $\Delta\theta$ divided by the static rotation θ_s as a function of the number of cycles N measured in test No. 17 ($D_{r0} = 38$ %, $\zeta_b = 0.4$ and $\zeta_c = 0$) and obtained from the simulations with and without consideration of the installation process, respectively*

From Fig. 12, it can be concluded that the simulation without consideration of the installation process overestimates the accumulated rotation measured in the experiment. The simulation incorporating the installation on the other hand reproduces the measurements very well. The simulation without installation predicts approximately 50 % higher values of $\Delta\theta/\theta_s$ at the end of the test compared to the measurements as well as compared to the simulation with incorporation of the installation process.

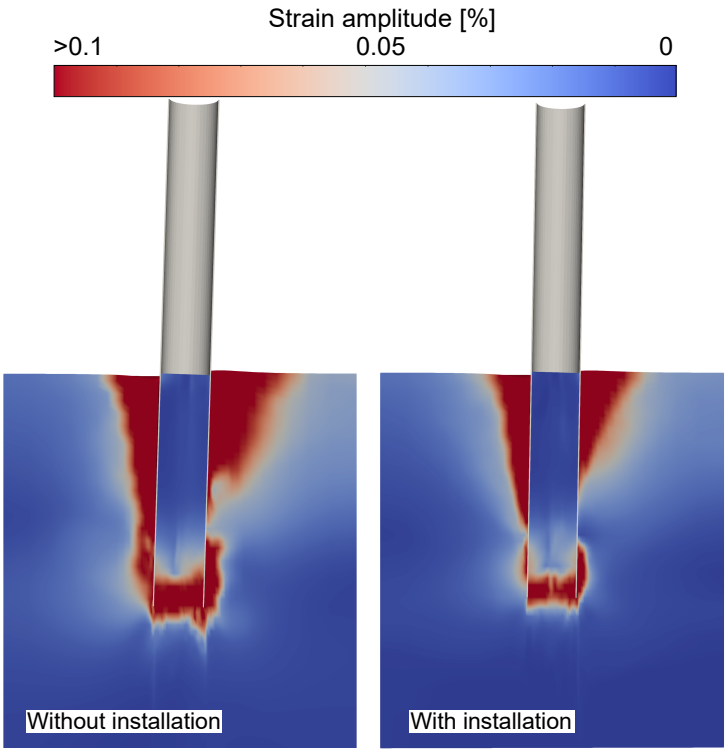

Figure 13: *Deformed shape and spatial field of the strain amplitude after the second loading cycle for test No. 17 and the simulations with and without consideration of the installation process, respectively. No deformation-scale factor is used.*

The spatial field of the strain amplitude for the simulations with and without incorporation of the installation, respectively, is given in Fig. 13 for test No. 17. Note that the deformed state after application of the second load cycle is displayed. It is evident that the area with strain amplitudes larger than 0.1 % is greater at both sides of the pile in case of the simulation without installation compared to the simulation with consideration of the installation-induced changes in the soil state. Since higher values of the strain amplitude result in higher rates of strain accumulation calculated by the HCA model (disproportionate relationship with the exponent $C_{\text{ampl}} = 1.7$), larger accumulation rates are predicted in the simulation without consideration of the installation process leading to a larger pile rotation.

The spatial field of relative density after the application of 10,000 loading cycles for the simulations with and without installation, respectively, is given for test No. 17 in Fig. 14. The deformed configuration is displayed. No deformation-scaling factor is used. The increased pile rotation in case of the simulation without consideration of the installation process is well visible in comparison to the simulation incorporating the installation process. In both cases a strong decrease in soil density accompanied by a heave of the soil around the pile at the ground surface is predicted by the simulations. The heave is slightly greater in case of the simulation without consideration of the installation process. While the relative density in the top half of the model is similar for both calculations, much higher D_r values are present in the vicinity of the pile tip in case of the simulation incorporating the installation process. As discussed previously based on Fig. 9 this high density is caused by the installation process of the pile. The density distribution in the vicinity of the pile tip is hardly changed by the application of the 10,000 loading cycles, so that the installation-induced changes in the soil state are still well visible. With ongoing cyclic loading the influence of the installation is assumed to decrease and the spatial fields of density and stress of the simulation without and with installation, respectively, equalize, as has been shown in (Staubach et al., 2020c). In the study presented in (Staubach et al., 2020c), however, 5 million loading

cycles were applied. Therefore, this aforementioned equalization may take several million load cycles to occur.

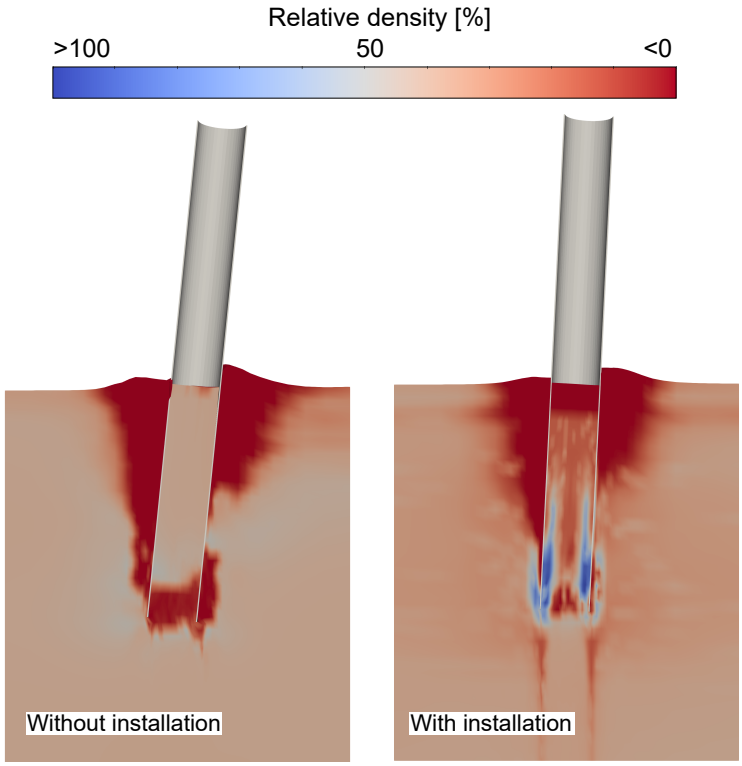

Figure 14: *Deformed shape and spatial field of the relative density after application of 10,000 cycles for test 17 and the simulations without and with consideration of the installation process, respectively. No deformation-scale factor is used.*

For the further model tests studied in the following only the accumulated rotation will be evaluated since the observations made from the spatial fields of strain amplitude and relative density at the end of the cyclic loading are similar to those discussed for test No. 17.

The results for test No. 18 ($D_{r0} = 38$ %, $\zeta_b = 0.52$ and $\zeta_c = 0$) in terms of $\Delta\theta/\theta_s$ versus N are given in Fig. 15. Note that the simulation without considering installation aborted due to the large deformations towards the end of the simulation ($N \approx 5,000$). Similar to test No. 17, the simulation without incorporation of the installation process overestimates the accumulated pile rotation. The simulation with installation reproduces the measured values well. The simulation without consideration of the installation process predicts approximately 45 % higher values for $\Delta\theta/\theta_s$ at $N \approx 5,000$ in comparison to the simulation incorporating the installation process. Compared to the measurements, the simulation neglecting the installation process shows values being 50 % higher at $N \approx 5,000$.

The results for test No. 8 with a very low initial relative density ($D_{r0} = 4$ %, $\zeta_b = 0.34$ and $\zeta_c = 0$) are displayed in Fig. 16. In accordance with the previous findings from the tests with an initial relative density of $D_{r0} = 38$ % a higher accumulation of rotation is observed for the simulation without consideration of the installation. The simulation with incorporation of the installation process reproduces the measurements well. Compared to the tests with higher initial density ($D_{r0} = 38$ %) the difference between the two simulation types is considerably larger for $D_{r0} = 4$ %.

The results for the one-way loading test with the lowest amplitude and an initial relative density of $D_{r0} = 38$ % (test No. 16, $\zeta_b = 0.27$ and $\zeta_c = 0$) are provided in Fig. 17. Both types of simulations overestimate the accumulated pile rotation for $N > 10$. This is more pronounced in case of the simulation without incorporation of the installation process. The simulation incorporating the installation process

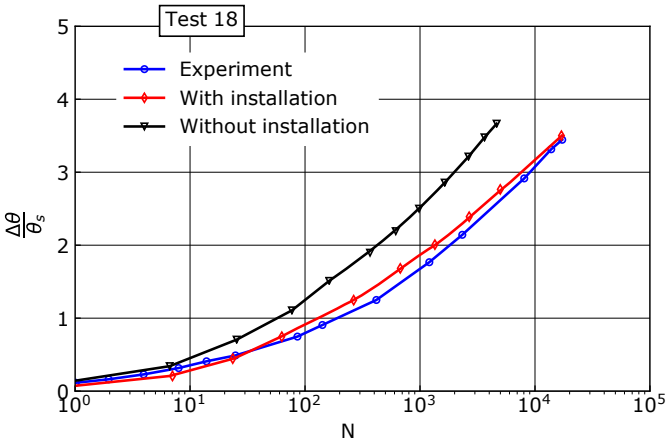

Figure 15: *Change of rotation $\Delta\theta$ divided by the static rotation θ_s versus number of cycles N measured in test No. 18 ($D_{r0} = 38$ %, $\zeta_b = 0.52$ and $\zeta_c = 0$) and obtained from the simulations with and without consideration of the installation process, respectively*

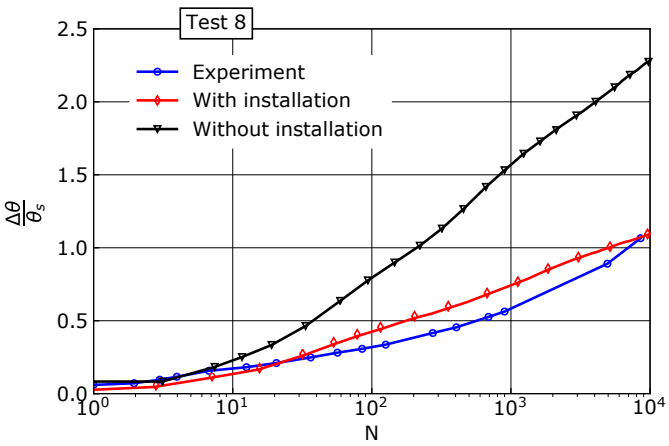

Figure 16: *Change of rotation $\Delta\theta$ divided by the static rotation θ_s versus number of cycles N measured in test No. 8 ($D_{r0} = 4$ %, $\zeta_b = 0.34$ and $\zeta_c = 0$) and obtained from the simulations with and without consideration of the installation process, respectively*

predicts approximately 50 % larger values of $\Delta\theta/\theta_s$ at $N \approx 10,000$ compared to the measurements. Likewise, the simulation without consideration of the installation process overestimates $\Delta\theta/\theta_s$ by almost 100 %. The difference between both types of simulations at $N \approx 10,000$ is approximately 30 %. Compared to the tests with higher cyclic loading amplitude (tests Nos. 17 and 18), the differences between the two simulation types are smaller for test No. 16 where a much lower cyclic amplitude has been applied.

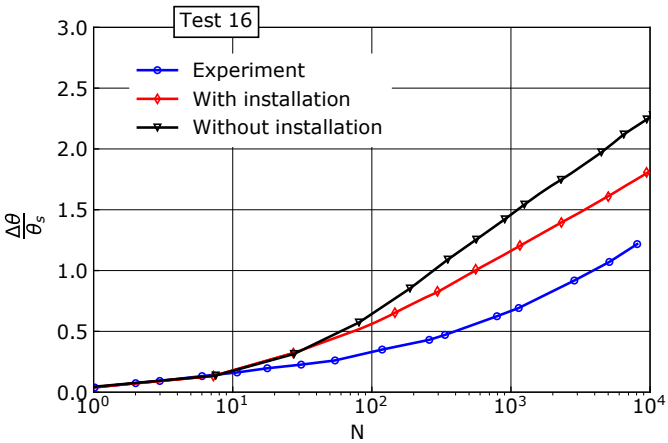

Figure 17: *Change of rotation $\Delta\theta$ divided by the static rotation θ_s versus number of cycles N measured in test No. 16 ($D_{r0} = 38$ %, $\zeta_b = 0.27$ and $\zeta_c = 0$) and obtained from the simulations with and without consideration of the installation process, respectively*

The results of the simulations of the test No. 20 ($D_{r0} = 38$ %, $\zeta_b = 0.4$ and $\zeta_c = -0.8$) are given in Fig. 18. Similar to the previous tests, the simulation without incorporation of the installation predicts larger rotation accumulation compared to the measurements. The simulation with consideration of the installation process leads to a better agreement with the results of the experiment. Compared to test No. 17, where $\zeta_b = 0.4$ was used as well but one-way cyclic loading was applied, the difference between both types of simulations is smaller. Towards the end of the test at $N = 1000$ both simulations give approximately the same value for $\Delta\theta/\theta_s$.

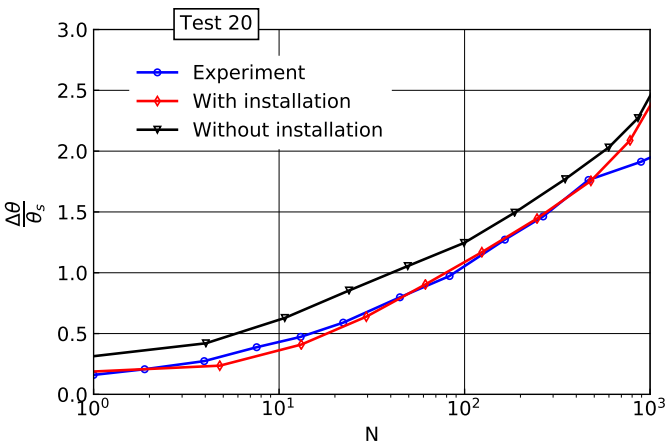

Figure 18: *Change of rotation $\Delta\theta$ divided by the static rotation θ_s versus number of cycles N measured in test No. 20 ($D_{r0} = 38$ %, $\zeta_b = 0.4$ and $\zeta_c = -0.8$) and obtained from the simulations with and without consideration of the installation process, respectively*

It is worth mentioning that the qualitative differences between the simulations incorporating the installation and the wished-in-place simulations were similar for the study of real-scale piles in case of initially

medium dense sand reported in (Staubach et al., 2020c). Thus, the large differences between the two simulation types (with and without installation, respectively) is not restricted to small-scale model tests as considered in the present study.

7 Conclusions and Outlook

7.1 Conclusions

The back-analysis of model tests on the long-term cyclic behaviour of piles performed by Leblanc et al. (Leblanc et al., 2010) showed that the incorporation of the installation process in the numerical simulations has a distinct impact on the predicted pile response under subsequent monotonic or cyclic lateral loading. The simulations without consideration of the installation process strongly overestimated the rotation of the pile subjected to monotonic lateral loading. The simulations incorporating the installation-induced changes of soil state lead to a better accordance with the measurements and higher pile resistance.

The cyclic loading tests with up to 20,000 cycles revealed that the accumulated pile rotation is influenced by the installation process as well. The simulations neglecting the installation-induced changes of soil state overestimated the pile rotation compared to the measurements. The simulations with incorporation of the installation process lead to a better agreement with the experimental results and exhibited less accumulation compared to the simulations without considering the installation process. The influence of the installation on the accumulated pile rotation was found to be smaller in case of cyclic loading tests with lower amplitude, while it increased with decreasing initial relative density prior to the installation.

In addition to the investigation of the influence of the installation effects, the study also shows that the HCA model in combination with the hypoplastic model with intergranular strain extension is able to predict the measurements in the model tests reasonably well, even though the parameters of the constitutive models have been determined from laboratory tests with higher stress level compared to the model tests (all hypoplastic parameters and the parameters C_{N1}, C_{N2} and C_{N3} of the HCA model) or have been estimated based on correlations with the grain size distribution curve or simple index properties (parameters C_{ampl}, C_e, C_p and C_Y of the HCA model).

The present study shows that a validation of numerical methods based on pile loading model tests should account for the installation-induced changes in the soil state in order to capture the initial soil conditions correctly. Therefore, model tests should be performed without a realistic installation of the pile (e.g. by placing the soil around the pile) if they are used for numerical back-analysis using methods in which the installation process is not simulated. If the pile installation was considered in the model tests and a full simulation of the installation process is not possible (e.g. because of the complexity of the required numerical tools), simplified approaches based e.g. on cavity expansion models (see e.g. (Schmüdderich et al., 2020)) or hybrid approaches, where only a small part of the installation is considered (Murphy et al., 2018), could be used to estimate the installation-induced changes of soil state.

7.2 Outlook

As has already been mentioned in the section presenting the parameter calibration, a determination of all HCA model parameters based on drained high-cyclic triaxial tests on yellow Leighton-Buzzard sand should be performed in order to investigate if some of the discrepancies between the simulations and the measurements discussed in Section 6 are caused by suboptimal parameters. In addition, the calibration should be based on triaxial tests performed at much lower stress level, similar to the stress level of the model tests. Up to now it is not clear if the parameters calibrated based on laboratory tests with high

stress level (50 to 300 kPa are usually applied in such tests) can be directly adopted for simulations involving considerably lower stress levels (0 to 5 kPa in the present case).

Field and centrifuge tests with realistic stress level considering pile installation with subsequent cyclic lateral loading as e.g. performed by (Rudolph, 2015) will be considered for the further validation of the simulation of the installation process and the HCA model. In addition, model tests performed in saturated sand will be back-analyzed as the influence of the installation process strongly depends on the drainage conditions as has been shown in (Staubach et al., 2020c; Staubach et al., 2020b). Furthermore, vibratory pile driving will be studied as it is believed that this installation technique will be applied in practice more frequently in the future. Based on previous research and the results of simulations of vibratory pile driving in saturated sand (see e.g. (Staubach et al., 2020a)), the installation-induced soil changes are believed to lead to opposite effects in terms of pile response to lateral loading compared to the tendencies reported in this work using jacking or impact driving.

Conflict of interest

The authors declare that they have no conflict of interest.

A Equations of the hypoplastic model with intergranular strain extension

The stress rate $\dot{\boldsymbol{\sigma}}$ is calculated from

$$\dot{\boldsymbol{\sigma}} = \mathsf{M} : \dot{\boldsymbol{\varepsilon}} \tag{12}$$

where $\dot{\boldsymbol{\varepsilon}}$ is the strain rate. The stiffness tensor M is defined by (Niemunis and Herle, 1997)

$$\mathsf{M} = \Big(\rho^{\chi} m_T + (1-\rho^{\chi}) m_R\Big)\mathsf{L} + \begin{cases} \rho^{\chi}(1-m_T)\mathsf{L} : \vec{\mathbf{h}} \otimes \vec{\mathbf{h}} + \rho^{\chi}\mathbf{N}\vec{\mathbf{h}} & \text{for} \quad \vec{\mathbf{h}} : \dot{\boldsymbol{\varepsilon}} > 0 \\ \rho^{\chi}(m_R - m_T)\mathsf{L} : \vec{\mathbf{h}} \otimes \vec{\mathbf{h}} & \phantom{\text{for}} \quad \vec{\mathbf{h}} : \dot{\boldsymbol{\varepsilon}} \leq 0 \end{cases} \tag{13}$$

with the intergranular strain tensor $\mathbf{h}$, its degree of mobilization ρ and its direction $\vec{\mathbf{h}}$ defined as

$$\rho = \frac{\|\mathbf{h}\|}{R} \quad \text{and} \quad \vec{\mathbf{h}} = \frac{\mathbf{h}}{\|\mathbf{h}\|}. \tag{14}$$

χ, m_T, m_R and R are material parameters controlling the influence of the intergranular strain. The evolution law of the intergranular strain $\mathbf{h}$ is (Niemunis and Herle, 1997)

$$\overset{\circ}{\mathbf{h}} = \begin{cases} (\mathsf{I} - \vec{\mathbf{h}} \otimes \vec{\mathbf{h}}\rho^{\beta_r}) : \dot{\boldsymbol{\varepsilon}} & \text{for} \quad \vec{\mathbf{h}} : \dot{\boldsymbol{\varepsilon}} > 0 \\ \dot{\boldsymbol{\varepsilon}} & \phantom{\text{for}} \quad \vec{\mathbf{h}} : \dot{\boldsymbol{\varepsilon}} \leq 0 \end{cases} \tag{15}$$

where β_R is another material parameter and I is the fourth-order identity tensor. The stiffness tensors L and $\mathbf{N}$ are given by the following equations (Wolffersdorff, 1996):

$$\mathsf{L} = f_b f_e \frac{1}{\mathrm{tr}(\hat{\boldsymbol{\sigma}} \cdot \hat{\boldsymbol{\sigma}})} (F^2 \mathsf{I} + a^2 \hat{\boldsymbol{\sigma}} \otimes \hat{\boldsymbol{\sigma}}) \tag{16}$$

$$\mathbf{N} = f_b f_e f_d \frac{Fa}{\mathrm{tr}(\hat{\boldsymbol{\sigma}} \cdot \hat{\boldsymbol{\sigma}})} (\hat{\boldsymbol{\sigma}} + \hat{\boldsymbol{\sigma}}^*) \tag{17}$$

Therein $\hat{\boldsymbol{\sigma}} = \dfrac{\boldsymbol{\sigma}}{\mathrm{tr}\boldsymbol{\sigma}}$ and $\hat{\boldsymbol{\sigma}}^* = \hat{\boldsymbol{\sigma}} - \frac{1}{3}\mathbf{I}$ are used. The scalar factors are defined by

$$a = \frac{\sqrt{3}(3 - \sin\varphi_c)}{2\sqrt{2}\sin\varphi_c} \ , \ f_d = \left(\frac{e - e_d}{e_c - e_d}\right)^{\alpha} \ , \ f_e = \left(\frac{e_c}{e}\right)^{\beta} \tag{18}$$

and

$$f_b = \frac{h_s}{n} \left(\frac{e_{i0}}{e_{c0}}\right)^{\beta} \frac{1 + e_i}{e_i} \left(\frac{3p}{h_s}\right)^{1-n} \left[3 + a^2 - a\sqrt{3}\left(\frac{e_{i0} - e_{d0}}{e_{c0} - e_{d0}}\right)^{\alpha}\right]^{-1}. \tag{19}$$

φ_c, h_s, n, e_{i0}, e_{d0}, e_{c0}, α and β are parameters and e is the actual void ratio. The pressure-dependent void ratios e_i, e_c and e_d in Eq. (18), describing the loosest, the critical and the densest state, are calculated using the following relation (Bauer, 1992)

$$\frac{e_i}{e_{i0}} = \frac{e_c}{e_{c0}} = \frac{e_d}{e_{d0}} = \exp\left[-\left(\frac{3p}{h_s}\right)^n\right]. \tag{20}$$

p is the mean effective stress. The scalar factor F in Eq. (16) and Eq. (17) is given by

$$F = \sqrt{\frac{1}{8}\tan(\psi)^2 + \frac{2 - \tan(\psi)^2}{2 + \sqrt{2}\tan(\psi)\cos(3\theta)}} - \frac{1}{2\sqrt{2}}\tan(\psi), \tag{21}$$

with $\tan(\psi) = \sqrt{3}\|\hat{\boldsymbol{\sigma}}^*\|$ and

$$\cos(3\theta) = -\sqrt{6}\frac{\mathrm{tr}(\hat{\boldsymbol{\sigma}}^* \cdot \hat{\boldsymbol{\sigma}}^* \cdot \hat{\boldsymbol{\sigma}}^*)}{[\mathrm{tr}(\hat{\boldsymbol{\sigma}}^* \cdot \hat{\boldsymbol{\sigma}}^*)]^{3/2}}. \tag{22}$$

B Influence of the installation method: jacking vs. impact driving

In order to investigate how large the assumption of a pile installation via jacking rather than impact driving influences the lateral loading behaviour of the pile, an additional simulation of the installation of the pile in sand with a relative density of $D_{r0} = 38$ % is performed. In this simulation the pile is jacked to an embedment depth of 0.288 m (80 % of the final depth) and then impact-driven until the final depth of 0.36 m is reached. A simulation of the complete installation by impact driving is not possible due to the huge and thus infeasible calculation times. The idea to simulate only parts of the installation process using impact driving has been adopted from (Fan, 2020; Fan et al., 2020). As mentioned beforehand, the driving force used in the experiments performed by Leblanc et al. (Leblanc et al., 2010) is unknown. However, Richards et al. (Richards et al., 2019) have performed very similar tests at the same institute

(Oxford University) using almost identical geometrical specifications for the model tests. For these tests the driving force is known and has been adopted for the simulation of the tests by Leblanc et al. as well. The only additional assumptions necessary are the impact duration (which is taken to be 0.01 s) and the frequency (assumed to be 1 Hz). The drop height was 0.3 m and the falling weight was 1.4 kg. After simulation of the installation using the procedure described above the resulting distributions of state variables have been transferred to the Lagrangian model. With this model the monotonic loading test has been simulated afterwards. Note that the state variables have been transferred for a state with inactive impact force. The results of the monotonic loading test displayed in Fig. 19 show that the results of the simulations are not strongly influenced by the installation method. The impact-driven pile exhibits only a slightly higher resistance towards the end of the test. Therefore, the assumption of an installation using jacking for all simulations of the model tests seems justified in the present case.

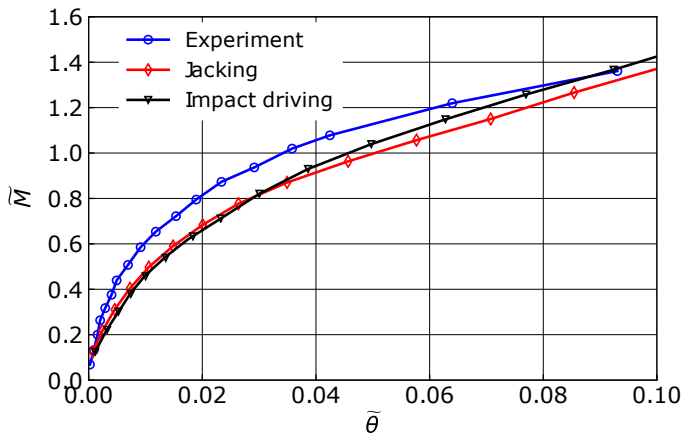

Figure 19: *Results of the monotonic loading test with an initial relative density of $D_{r0} = 38$ %: Development of non-dimensional moment $\tilde{M}$ with non-dimensional rotation $\tilde{\theta}$ measured in the experiment and obtained from the simulations using jacking and impact driving, respectively*

C Installation-induced changes of soil state in case of the tests with an initial relative density of $D_{r0} = 4$ %

The change in relative density during jacking of the pile for the test with an initial relative density of $D_{r0} = 4$ % is shown for different stages of the installation process in Fig. 20. Similar to the test with an initial relative density of $D_{r0} = 38$ %, a strong compaction of the soil in the vicinity of the pile tip is observed. This compaction is more pronounced inside of the pile compared to the outside. In terms of compacted area the results of the simulations with the two different relative densities ($D_{r0} = 4$ % or 38 %) are comparable. Opposite to the tests with $D_{r0} = 38$ %, no loosening of the soil near the ground surface occurs as the soil is already in its loosest possible state. The development of mean effective stress during driving for $D_{r0} = 4$ % is shown in Fig. 21. The spatial distribution is similar to the test with $D_{r0} = 38$ % for all stages of the installation process. For the depths $t = 8/16/24$ cm the test with $D_{r0} = 4$ % shows a slightly larger area with pressures greater than 100 kPa compared to the test with $D_{r0} = 38$ %.

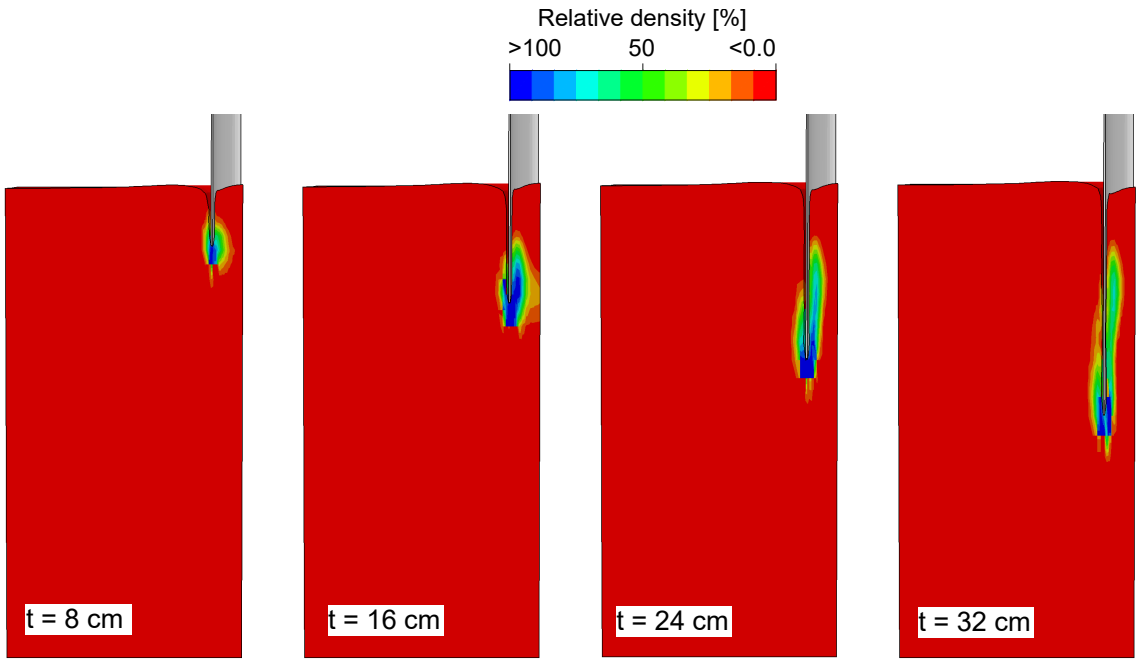

Figure 20: *Development of relative density during the driving process in case of the test with an initial relative density of* $D_{r0} = 4$ *%*

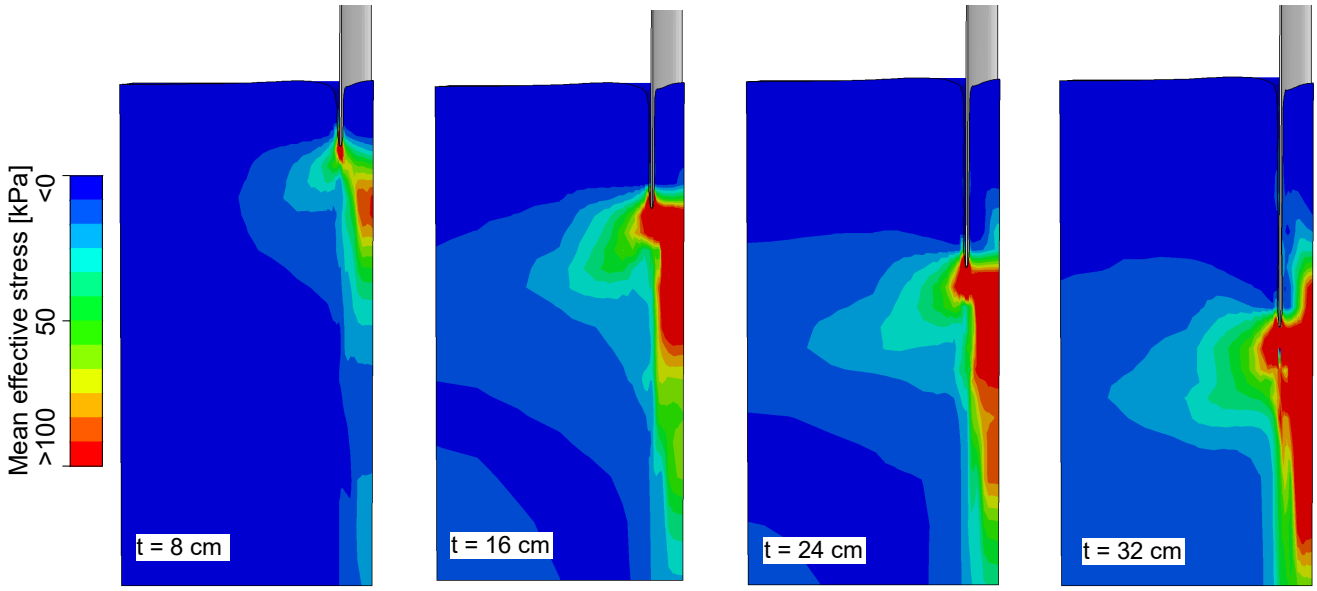

Figure 21: *Development of mean effective stress during the driving process in case of the test with an initial relative density of* $D_{r0} = 4$ *%*

References

Achmus, M., Y.-S. Kuo, and K. Abdel-Rahman (2009). "Behavior of monopile foundations under cyclic lateral load". In: *Computers and Geotechnics* 36, pp. 725–735.

Arshad, M. and B. C. O. Kelly (2017). "Model Studies on Monopile Behavior under Long-Term Repeated Lateral Loading". In: *International Journal of Geomechanics* 17.1, p. 04016040. DOI: 10.1061/(ASCE)GM.1943-5622.0000679.

Bauer, E. (1992). *Zum mechanischen Verhalten granularer Stoffe unter vorwiegend ödometerischer Beanspruchu* Dissertation, Institut für Bodenmechanik und Felsmechanik der Universität Fridericiana in Karlsruhe, Heft Nr. 130.

Bayton, S., J. Black, and R. T. Klinkvort (2018). "Centrifuge modelling of long term cyclic lateral loading on monopiles". In: *9th International Conference on Physical Modelling in Geotechnics*, pp. 689–694.

Benson, D. J. (1992). "Computational methods in Lagrangian and Eulerian hydrocodes". In: *Computer Methods in Applied Mechanics and Engineering* 99.2, pp. 235–394. ISSN: 0045-7825.

Benson, D. J. and S. Okazawa (2004). "Contact in a multi-material Eulerian finite element formulation". In: *Computer Methods in Applied Mechanics and Engineering* 193.39. The Arbitrary Lagrangian-Eulerian Formulation, pp. 4277–4298. ISSN: 0045-7825.

Carstensen, A., T. Pucker, and J. Grabe (2018). "Numerical model to predict the displacement of piles under cyclic lateral loading using a new hypoplastic spring element". In: *Computers and Geotechnics* 101, pp. 217–223. ISSN: 0266-352X. DOI: https://doi.org/10.1016/j.compgeo.2018.05.001.

Chrisopoulos, S. and J. Vogelsang (2019). "A finite element benchmark study based on experimental modeling of vibratory pile driving in saturated sand". In: *Soil Dynamics and Earthquake Engineering* 122, pp. 248–260. ISSN: 0267-7261. DOI: https://doi.org/10.1016/j.soildyn.2019.01.001.

Cuéllar, P., P. Mira, M. Pastor, J. Fernández Merodo, M. Baeßler, and W. Rücker (2014). "A numerical model for the transient analysis of offshore foundations under cyclic loading". In: *Computers and Geotechnics* 59, pp. 75–86.

Daryaei, R., M. Bakroon, D. Aubram, and F. Rackwitz (2020). "Numerical evaluation of the soil behavior during pipe-pile installation using impact and vibratory driving in sand". In: *Soil Dynamics and Earthquake Engineering* 134, p. 106177. ISSN: 0267-7261. DOI: https://doi.org/10.1016/j.soildyn.2020.106177.

Fan, S., B. Bienen, and M. Randolph (2019). "Centrifuge study on effect of installation method on lateral response of monopiles in sand". In: *International Journal of Physical Modelling in Geotechnics* 0.0, pp. 1–13. DOI: 10.1680/jphmg.19.00013.

Fan, S., B. Bienen, and M. Randolph (2020). "Effects of pile installation on subsequent response under lateral loading, Part I: Pile installation". In: *Journal of Geotechnical and Geoenvironmentral Engineering*. ISSN: 0733-9410.

Fan, S. (2020). "Effect of the installation process on the subsequent response of monopiles under lateral loading in sand". English. PhD thesis. The University of Western Australia. DOI: 10.26182/3dyy-r158.

Galavi, V., M. Martinelli, A. Elkadi, P. Ghasemi, and R. Thijssen (Sept. 2019). "Numerical simulation of impact driven offshore monopiles using the material point method". In: *Proceedings of the XVII ECSMGE-2019*. DOI: 10.32075/17ECSMGE-2019-0758.

Gourvenec, S. and M. Randolph (Jan. 2011). *Offshore Geotechnical Engineering*. ISBN: ISBN 13: 9780415477444 ISBN 10: 0415477441. DOI: 10.1201/9781315272474.

Grandas-Tavera, C., J. Vogelsang, and T. Triantafyllidis (2019). "Simplified simulation of the installation of vibro-piles in water saturated soil". In: *Soil Dynamics and Earthquake Engineering* 121, pp. 491–498. ISSN: 0267-7261. DOI: https://doi.org/10.1016/j.soildyn.2018.11.011.

Hamann, T., G. Qiu, and J. Grabe (2015). "Application of a Coupled Eulerian-Lagrangian approach on pile installation problems under partially drained conditions". In: *Computers and Geotechnics* 63, pp. 279–290. DOI: https://doi.org/10.1016/j.compgeo.2014.10.006.

Herle, I. (1997). *Hypoplastizität und Granulometrie einfacher Korngerüste.* Dissertation, Institut für Bodenmechanik und Felsmechanik der Universität Fridericiana in Karlsruhe, Heft Nr. 142.

Jostad, H. P., B. Dahl, A. Page, N. Sivasithamparam, and H. Sturm (2020). "Evaluation of soil models for improved design of offshore wind turbine foundations in dense sand". In: *Géotechnique* 70.8, pp. 682–699. DOI: 10.1680/jgeot.19.TI.034.

Kim, K., B. Nam, and H. Youn (Sept. 2015). "Effect of Cyclic Loading on the Lateral Behavior of Offshore Monopiles Using the Strain Wedge Model". In: *Mathematical Problems in Engineering* 2015, pp. 1–12. DOI: 10.1155/2015/485319.

Kimmig, I., T. Triantafyllidis, and L. Knittel (2019). "Experimentelle, analytische und numerische Untersuchungen zur Verdichtungsprognose von Sand bei der Rütteldruckverdichtung". In: *Bautechnik* 96.10, pp. 760–772. DOI: 10.1002/bate.201900038.

Leblanc, C., G. Houlsby, and B. Byrne (2010). "Response of stiff piles in sand to long-term cyclic lateral loading". In: *Géotechnique* 60.2, pp. 79–90.

Li, S., Y. Zhang, and H. P. Jostad (2019). "Drainage conditions around monopiles in sand". In: *Applied Ocean Research* 86, pp. 111–116. ISSN: 0141-1187. DOI: https://doi.org/10.1016/j.apor.2019.01.024.

Li, Z., S. Haigh, and M. Bolton (2010). "Centrifuge modelling of mono-pile under cyclic lateral loads". In: *Physical Modelling in Geotechnics* 2, pp. 965–970.

Liu, H. Y., J. A. Abell, A. Diambra, and F. Pisanò (2019). "Modelling the cyclic ratcheting of sands through memory-enhanced bounding surface plasticity". In: *Géotechnique* 69.9, pp. 783–800. DOI: 10.1680/jgeot.17.P.307.

Machacek, J., T. Triantafyllidis, and P. Staubach (2018). "Fully coupled simulation of an opencast mine subjected to earthquake loading". In: *Soil Dynamics and Earthquake Engineering* 115, pp. 853–867. ISSN: 0267-7261. DOI: https://doi.org/10.1016/j.soildyn.2018.09.016.

Machaček, J., T. Wichtmann, H. Zachert, and T. Triantafyllidis (2018). "Long-term settlements of a ship lock: measurements vs. FE-prediction using a high cycle accumulation model". In: *Computers and Geotechnics* 97.5, pp. 222–232.

Machaček, J. (2020). "Contributions to the numerical modeling of saturated and unsaturated soils". PhD thesis. Veröffentlichung des Instituts für Bodenmechanik und Felsmechanik am Karlsruher Institut für Technologie (KIT).

Murphy, G., D. Igoe, P. Doherty, and K. Gavin (2018). "3D FEM approach for laterally loaded monopile design". In: *Computers and Geotechnics* 100, pp. 76–83. ISSN: 0266-352X. DOI: https://doi.org/10.1016/j.compgeo.2018.03.013.

Nagula, S. and J. Grabe (July 2020). "Coupled Eulerian Lagrangian based numerical modelling of vibro-compaction with model vibrator". In: *Computers and Geotechnics* 123, p. 103545. DOI: 10.1016/j.compgeo.2020.103545.

Niemunis, A. (2008). *Incremental Driver User's manual.* available from www.pg.gda.pl/∼aniem/anliter.html.

Niemunis, A. and I. Herle (1997). "Hypoplastic model for cohesionless soils with elastic strain range". In: *Mechanics of Cohesive-Frictional Materials* 2.4, pp. 279–299.

Niemunis, A. and I. Melikayeva (2015). "Improved Integration of High-Cycle Accumulated Strain Using Hierarchical and EAS Finite Elements". In: *Holistic Simulation of Geotechnical Installation Processes:*

Numerical and Physical Modelling. Ed. by T. Triantafyllidis. Cham: Springer International Publishing, pp. 181–205.

Niemunis, A., T. Wichtmann, and T. Triantafyllidis (2005). "A high-cycle accumulation model for sand". In: *Computers and Geotechnics* 32.4, pp. 245–263.

Osinov, V., S. Chrisopoulos, and C. Grandas-Tavera (Oct. 2016). "Vibration-Induced Stress Changes in Saturated Soil: A High-Cycle Problem". In: *Holistic Simulation of Geotechnical Installation Processes: Benchmarks and Simulations*. Vol. 80, pp. 69–84. ISBN: 978-3-319-23158-7.

Page, A. M., G. Grimstad, G. R. Eiksund, and H. P. Jostad (2019). "A macro-element model for multi-directional cyclic lateral loading of monopiles in clay". In: *Computers and Geotechnics* 106, pp. 314–326. ISSN: 0266-352X. DOI: `https://doi.org/10.1016/j.compgeo.2018.11.007`. URL: `http://www.sciencedirect.com/science/article/pii/S0266352X18302866`.

Page, A. M., R. T. Klinkvort, S. Bayton, Y. Zhang, and H. Jostad (Sept. 2020). "A procedure for predicting the permanent rotation of monopiles in sand supporting offshore wind turbines". In: *Marine Structures* 75. DOI: `10.1016/j.marstruc.2020.102813`.

Phuong, N., F. Tol, A. Elkadi, and A. Rohe (May 2014). "Modelling of pile installation using the material point method (MPM)". In: *Numerical Methods in Geotechnical Engineering*. Ed. by Hicks, Brinkgreve, and Rohe. DOI: `10.1201/b17017-50`.

Qiu, G., S. Henke, and J. Grabe (Jan. 2011). "Application of a Coupled Eulerian-Lagrangian Approach on Geomechanical Problems Involving Large Deformation". In: *Computers and Geotechnics* 38, pp. 30–39.

Richards, I. A., B. W. Byrne, and G. T. Houlsby (2019). "Monopile rotation under complex cyclic lateral loading in sand". In: *Géotechnique* 0.0, pp. 1–15. DOI: `10.1680/jgeot.18.P.302`.

Rudolph, C. (2015). "Untersuchungen zur Drift von Pfählen unter zyklischer, lateraler Last aus veränderlicher Richtung". PhD thesis. Veröffentlichungen des Instituts für Geotechnik und Baubetrieb der Technischen Universität Hamburg.

Rudolph, C., B. Bienen, and J. Grabe (2014). "Effect of variation of the loading direction on the displacement accumulation of large-diameter piles under cyclic lateral loading in sand". In: *Canadian Geotechnical Journal* 51.10, pp. 1196–1206.

Schmüdderich, C., M. Shahrabi, M. Taiebat, and A.Lavasan (2020). "Strategies for numerical simulation of cast-in-place piles under axial loading". In: *Computers and Geotechnics* 125, p. 103656. ISSN: 0266-352X. DOI: `https://doi.org/10.1016/j.compgeo.2020.103656`.

Solf, O. (2012). *Zum mechanischen Verhalten von zyklisch belasteten Offshore-Gründungen*. Dissertation, Veröffentlichungen des Institutes für Bodenmechanik und Felsmechanik am Karlsruher Institut für Technologie, Heft 176.

Staubach, P. and J. Machacek (2019). "Influence of relative acceleration in saturated sand: Analytical approach and simulation of vibratory pile driving tests". In: *Computers and Geotechnics* 112, pp. 173–184. ISSN: 0266-352X. DOI: `https://doi.org/10.1016/j.compgeo.2019.03.027`.

Staubach, P., J. Machacek, J. Skowronek, and T. Wichtmann (2020a). "Vibratory pile driving in water-saturated sand: back-analysis of model tests using a hydro-mechanically coupled CEL method". In: *Soils and Foundations*. DOI: `https://doi.org/10.1016/j.sandf.2020.11.005`.

Staubach, P., J. Machacek, and T. Wichtmann (2020b). "Impact of the installation on the long-term behaviour of offshore wind turbine pile foundations". In: *4th International Symposium on Frontiers in Offshore Geotechnics,* In print. Taylor & Francis Group, London, UK.

Staubach, P., J. Machaček, M. Moscoso, and T. Wichtmann (2020c). "Impact of the installation on the long-term cyclic behaviour of piles in sand: A numerical study". In: *Soil Dynamics and Earthquake*

Engineering 138, p. 106223. ISSN: 0267-7261. DOI: https://doi.org/10.1016/j.soildyn.2020.106223.

Staubach, P. and T. Wichtmann (2020). "Long-term deformations of monopile foundations for offshore wind turbines studied with a high-cycle accumulation model". In: *Computers and Geotechnics* 124, p. 103553. ISSN: 0266-352X. DOI: https://doi.org/10.1016/j.compgeo.2020.103553.

Triantafyllidis, T. and I. Kimmig (2019). "A simplified model for vibro compaction of granular soils". In: *Soil Dynamics and Earthquake Engineering* 122, pp. 261–273. ISSN: 0267-7261. DOI: https://doi.org/10.1016/j.soildyn.2018.12.008.

Truong, P., B. M. Lehane, V. Zania, and R. T. Klinkvort (2019). "Empirical approach based on centrifuge testing for cyclic deformations of laterally loaded piles in sand". In: *Géotechnique* 69.2, pp. 133–145.

Wang, D., B. Bienen, M. N., Y. Tian, J. Zheng, T. Pucker, and M. F. Randolph (2015). "Large deformation finite element analyses in geotechnical engineering". In: *Computers and Geotechnics* 65, pp. 104–114. ISSN: 0266-352X. DOI: https://doi.org/10.1016/j.compgeo.2014.12.005.

White, D. J. and M. D. Bolton (2004). "Displacement and strain paths during plane-strain model pile installation in sand". In: *Géotechnique* 54.6, pp. 375–397. DOI: 10.1680/geot.2004.54.6.375.

Wichtmann, T. (2005). *Explicit accumulation model for non-cohesive soils under cyclic loading.* PhD thesis, Publications of the Institute of Soil Mechanics and Foundation Engineering, Ruhr-University Bochum, Issue No. 38.

Wichtmann, T., A. Niemunis, and T. Triantafyllidis (2005). "Strain accumulation in sand due to cyclic loading: drained triaxial tests". In: *Soil Dynamics and Earthquake Engineering* 25.12, pp. 967–979.

Wichtmann, T., A. Niemunis, and T. Triantafyllidis (2006). "Experimental evidence of a unique flow rule of non-cohesive soils under high-cyclic loading". In: *Acta Geotechnica* 1.1, pp. 59–73.

Wichtmann, T., A. Niemunis, and T. Triantafyllidis (2007a). "On the influence of the polarization and the shape of the strain loop on strain accumulation in sand under high-cyclic loading". In: *Soil Dynamics and Earthquake Engineering* 27.1, pp. 14–28.

Wichtmann, T., A. Niemunis, and T. Triantafyllidis (2007b). "Strain accumulation in sand due to cyclic loading: drained cyclic tests with triaxial extension". In: *Soil Dynamics and Earthquake Engineering* 27.1, pp. 42–48.

Wichtmann, T., A. Niemunis, and T. Triantafyllidis (2009). "Validation and calibration of a high-cycle accumulation model based on cyclic triaxial tests on eight sands". In: *Soils and Foundations* 49.5, pp. 711–728.

Wichtmann, T., A. Niemunis, and T. Triantafyllidis (2010a). "On the "elastic" stiffness in a high-cycle accumulation model for sand: a comparison of drained and undrained cyclic triaxial tests". In: *Canadian Geotechnical Journal* 47.7, pp. 791–805.

Wichtmann, T., A. Niemunis, and T. Triantafyllidis (2010b). "On the determination of a set of material constants for a high-cycle accumulation model for non-cohesive soils". In: *International Journal For Numerical And Analytical Methods in Geomechanics* 34.4, pp. 409–440.

Wichtmann, T., A. Niemunis, and T. Triantafyllidis (2013). "On the "elastic stiffness" in a high-cycle accumulation model - continued investigations". In: *Canadian Geotechnical Journal* 50.12, pp. 1260–1272.

Wichtmann, T., A. Niemunis, and T. Triantafyllidis (2014). "Flow rule in a high-cycle accumulation model backed by cyclic test data of 22 sands". In: *Acta Geotechnica* 9.4, pp. 695–709.

Wichtmann, T., A. Niemunis, and T. Triantafyllidis (2015). "Improved simplified calibration procedure for a high-cycle accumulation model". In: *Soil Dynamics and Earthquake Engineering* 70.3, pp. 118–132.

Wichtmann, T. and T. Triantafyllidis (2015). "Inspection of a high-cycle accumulation model for large numbers of cycles (N = 2 million)". In: *Soil Dynamics and Earthquake Engineering* 75, pp. 199–210.

Wolffersdorff, P.-A. von (1996). "A hypoplastic relation for granular materials with a predefined limit state surface". In: *Mechanics of Cohesive-Frictional Materials* 1.3, pp. 251–271.

Yang, Z., R. Jardine, B. Zhu, C. Tsuha, and P. Foray (2010). "Sand grain crushing and interface shearing during displacement pile installation in sand". In: *Géotechnique* 60.6, pp. 469–482. DOI: 10.1680/geot.2010.60.6.469.

Yang, Z. X., Y. Y. Gao, R. J. Jardine, W. B. Guo, and D. Wang (2020). "Large Deformation Finite-Element Simulation of Displacement-Pile Installation Experiments in Sand". In: *Journal of Geotechnical and Geoenvironmental Engineering* 146.6, p. 04020044. DOI: 10.1061/(ASCE)GT.1943-5606.0002271.

Yu, L.-Q., L.-Z. Wang, Z. Guo, S. Bhattacharya, G. Nikitas, L.-L. Li, and Y.-L. Xing (2015). "Long-term dynamic behavior of monopile supported offshore wind turbines in sand". In: *Theoretical and Applied Mechanics Letters* 5.2. Special Issue: Offshore Structure-Soil Interaction, pp. 80–84. ISSN: 2095-0349.

Zachert, H. (2015). *Zur Gebrauchstauglichkeit von Gründungen für Offshore-Windenergieanlagen.* Dissertation, Veröffentlichungen des Institutes für Bodenmechanik und Felsmechanik am Karlsruher Institut für Technologie, Heft Nr. 180.

Zachert, H., T. Wichtmann, P. Kudella, and T. Triantafyllidis (2020). "Inspection of a high-cycle accumulation model for sand based on recalculations of a full-scale test on a gravity base foundation for offshore wind turbines". In: *Computers and Geotechnics* 126, p. 103727. ISSN: 0266-352X. DOI: https://doi.org/10.1016/j.compgeo.2020.103727.

Zachert, H., T. Wichtmann, P. Kudella, T. Triantafyllidis, and U. Hartwig (2014). "Validation of a high cycle accumulation model via FE-simulations of a full-scale test on a gravity base foundation for offshore wind turbines". In: *International Wind Engineering Conference, IWEC 2014, Hannover.*

Zachert, H., T. Wichtmann, T. Triantafyllidis, and U. Hartwig (2015). "Simulation of a full-scale test on a Gravity Base Foundation for Offshore Wind Turbines using a High Cycle Accumulation Model". In: *3rd International Symposium on Frontiers in Offshore Geotechnics (ISFOG), Oslo.*